The mineralogy, petrography, and paragenesis of the polymetallic (Co-Ni-As-Au) veins

of the Nictaux Falls Dam Occurrence, Annapolis Valley, Nova Scotia

By Natalie Christine McNeil

A Thesis Submitted to
Saint Mary's University, Halifax, Nova Scotia
in Partial Fulfillment of the Requirements for
the Degree of Bachelor of Science

June, 2019, Halifax, Nova Scotia

Approved: Dr. Erin Adlakha
Supervisor

Approved: George O'Reilly
External Reviewer

Date: June 2, 2019

Contents

Figures

Tables

Appendix Petrography

Appendix Tables

7

The mineralogy, paragenesis, and petrogenesis of the polymetallic (Co-Ni-As-Au) veins

of the Nictaux Falls Dam Occurrence, Annapolis Valley, Nova Scotia

By Natalie Christine McNeil

Abstract

Cobalt occurrences in Nova Scotia are poorly understood and their association with five elements vein deposits is unclear. The Nictaux Falls polymetallic (Co-Ni-Au-Ag-Bi) vein occurrence is hosted in the spillway of the Nova Scotia Power Dam found along the Nictaux River, Annapolis County. The sulfarsenide mineralized quartz veins crosscut the Silurian-aged Kentville Formation metasediments, near its contact the Devono-Carboniferous South Mountain Batholith. Two main zones are identified, hosting two styles of mineralization: laminated sulfarsenide-quartz veins (MZ1) and quartz breccia veins containing sulfarsenide-mineralized wall rock clasts (MZ2). The laminated MZ1 veins are heterogeneous with euhedral sulfarsenides and coxcomb quartz occurring on opposite sides of the vein. Wall rock MZ2 clasts contain late net-texture sulfarsenides and quartz. Petrographic work identified a spatial relationship between sulfarsenides and wall rock gangue minerals (chlorite, biotite, rutile) in both styles. Both styles are characterized by early interstitial chlorite, biotite, and rutile, followed by rounded sulfide inclusions, and surrounded by compositionally zoned sulfarsenide (arsenopyrite, mantled by a secondary arsenopyrite, Fe-rich cobaltite, and Fe-Co-rich gersdorffite). Textural evidence using Micro-XRF imaging suggests the unidirectional zoning is a product of Rayleigh fractionation or a decrease in pH. Mafic intrusions present in the spillway and host metasediments were evaluated as potential metal sources. SEM-EDS analyses and S-isotope work tentatively suggest the metasediments are the most likely source of sulfur and metals for the NFDO. In situ SIMS work is required in order to identify possible event of fluid mixing between brines that equilibrated with the metasediments and marine brines of the Maritimes Basin. The NFDO comprises a unique mineral assemblage that could be an example of a five elements vein occurrence. Further studies of cobalt occurrences in the Meguma Terrane is required in order to understand cobalt metallogeny in Nova Scotia and possible five element vein occurrences in the province.

Date Submitted: June 2, 2019

Introduction

Cobalt is a strategic metal that is becoming increasingly needed due to its usage in several currently developing modern technologies. In particular, increased cobalt demand is driven by its use in battery cathodes and superalloys. The majority of the world's cobalt resources comes from the Republic of Congo; however, in that country it is not mined in an environmentally or ethically responsible way. The Cobalt-Gowganda region of Ontario has also been an important source of cobalt in the past. It is ethically important that countries explore and produce cobalt in an environmentally responsible manner. If cobalt mining in the Republic of Congo ceases, cobalt will only be mined elsewhere as a byproduct in Ni-Cu mines (e.g. Voiseys Bay, Labrador).

Sub-economic cobalt occurrences documented in the Meguma Terrane include the Nictaux Falls Dam Occurrence (NFDO), Cape St. Mary's, and Lansdowne (**Figure 1**; O'Reilly, 1992), as well as cobalt occurrences associated with IOCG type deposits along the Cobequid-Chedabucto Fault Zone (CCFZ). However, there is no association between the cobalt occurrences in the Meguma Terrane and the CCFZ. Currently, the cobalt metallogeny of Nova Scotia remains poorly understood and understudied. This study focuses on the Nictaux Falls Dam Occurrence in order to initiate interest and research on cobalt occurrences in Nova Scotia.

The NFDO is located in the spillway of the Nova Scotia Corporation hydro power dam along the Nictaux River in the Annapolis Valley south of Middleton, Annapolis County. (**Figure 1, Figure 2**). The occurrence was discovered by Shell Canadian Resources Limited in 1978 during a uranium exploration program (Black, 1978).
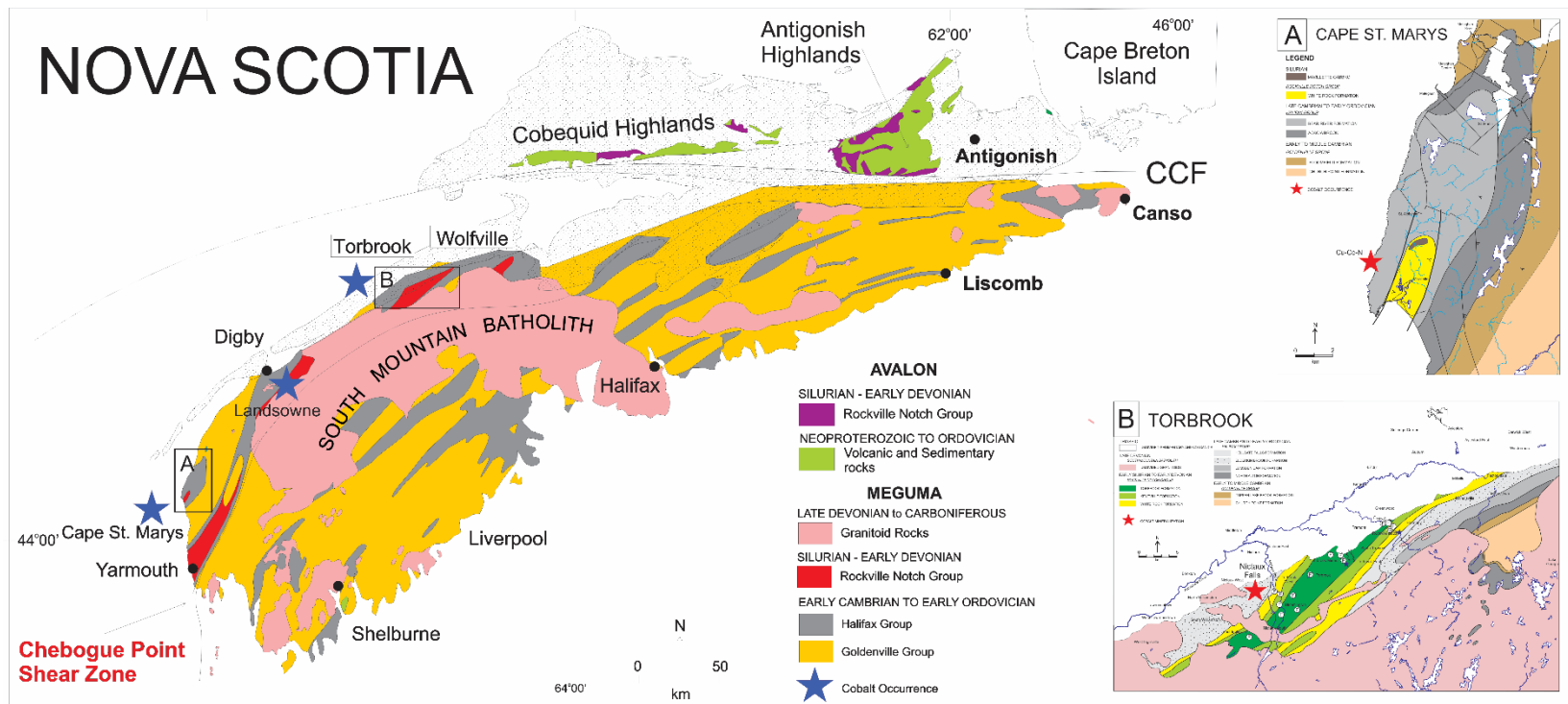
Figure 1: Map of Nova Scotia showing the locations of cobalt occurrences in the province. Modified from White et al., 2018.
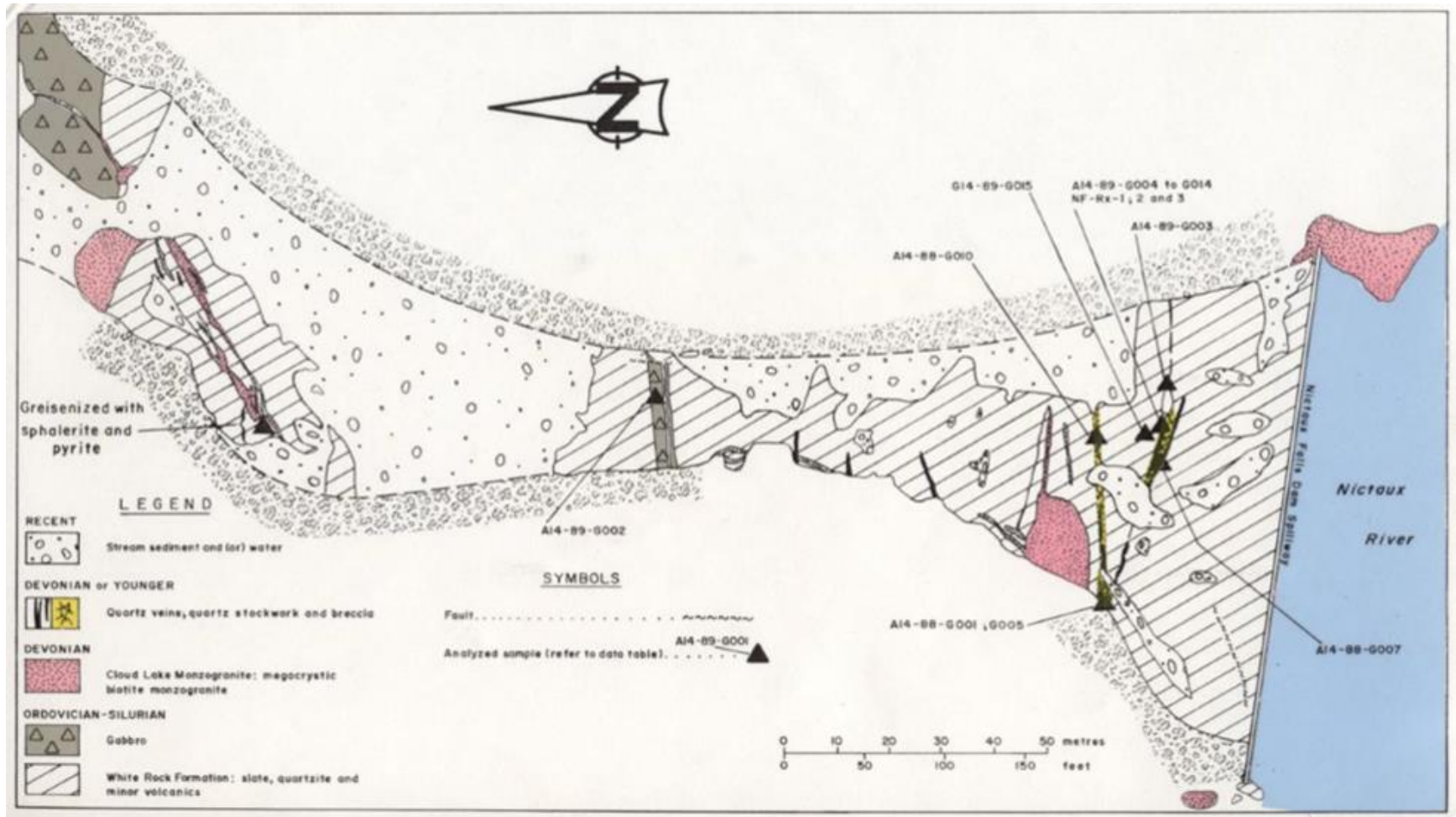
Figure 2: Representative field map constructed by O'Reilly (1992) showing the major lithologies and mineralized veins hosted in the Nictaux Falls Dam Occurrence, the Annapolis Valley, Nova Scotia

Preliminary fieldwork, mapping, and sampling were completed between 1988 and 1989 by George O'Reilly of Nova Scotia Department of Mines and Energy (**Figure 2**; subsequently the Department of Natural Resources). The occurrence is comprised of sulfarsenide mineralization (e.g. arsenopyrite and cobaltite) and native gold in quartz veins hosted in metasediments of the Silurian-age Kentville Formation near its contact with the Cloud Lake Pluton of the South Mountain Batholith (SMB) (O'Reilly, 1995; **Figure 2**). Low uranium is detected in the assays; however, no distinct association is identified between cobalt and uranium. Grab sample analyses returned anomalous concentrations of Co (up to 16200 ppm), Ni (up to 2840 ppm), As (up to 10 wt%), Bi (up to 90 ppm), and Au (up to 80 ppm) in the veins. O'Reilly (1995) suggested the elemental assemblage resembles that of five elements (Ag-Co-Ni-Bi-As) vein deposits and that local gabbroic intrusions and diabase sills may be the source of cobalt and nickel.

In 2006, the spillway was completely restructured and updated, exposing new bedrock. Besides O'Reilly's preliminary work, no detailed studies have been completed on the area. Details of vein mineralogy, formation conditions, and genetic relationships of the veins with the surrounding intrusions (e.g. SMB, gabbro, diabase) remained poorly understood. This thesis presents a combined field and microanalytical study on the NFDO and investigates: i) the timing and genetic relationship of the veins with the surrounding intrusions and host rocks through field mapping, ii) the mineral assemblages and paragenesis of the sulfarsenide veins through petrographic study, iii) the role of the gabbro and metasediments as a potential source of metals using lithogeochemistry and petrographic study, and iv) possible sources of sulfur using bulk sulfur isotope determinations. The results of this study are used to model the formation of the occurrence

and are compared to similar polymetallic vein deposits, such as five elements deposits, in Canada and worldwide.

Background Information

Based on the observed elemental assemblage, O'Reilly (1992) suggested that the NFDO could be a five elements vein deposit. However, it also has similarities to metasediment hosted Co-Cu-Au deposits. Five-elements (Ag-Co-Ni-Bi-As) vein deposits, such as in the Cobalt-Gowganda District (Ontario), are controversial hydrothermal vein deposits of a unique paragenesis, generally consisting of native metals (e.g. Ag, As, Bi) overprinted by Ni-, Co-, Fe- arsenides and hosted in late gangue (e.g. carbonates, fluorite, quartz) (e.g., Kissin, 1992). The mineral paragenesis is similar between deposits; however, the host rocks, alteration, fluid composition, age, temperature and pressure conditions are variable (e.g., Kissin, 1992; Markl et al. 2017). Considering this variability, emphasis has been placed on the vein mineralogy, textures, and paragenesis in order to classify five element vein deposits.

The ores in five elements vein deposits exhibit the following paragenesis: i) an early, low-grade sulfide stage (e.g. sphalerite, pyrite, chalcopyrite), followed by ii) a native element (Bi, Au, Ag) stage with or without arsenides/antimonides, iii) a arsenide/antimonide stage (e.g. safflorite and skutterudite) typically forming around native element aggregates, iv) a sulfarsenide stage, v) a later sulfide stage, and vi) a late gangue stage (e.g. typically carbonates, and rarely quartz, fluorite and barite) (e.g. Kissin, 1992; Markl et al., 2016). The native element minerals exhibit skeletal and dendritic textures, suggesting rapid growth under disequilbrium conditions in open space (Markl et al., 2016; Burisch et al., 2017). Arsenic occurs in three valence states, as native As (As^0), arsenides

(As^{1-}, As^{2-} As^{3-}) and sulfarsenates (As^{3+}), which indicates the importance of redox reactions during mineralization (Markl et al., 2016).

Mineral assemblages and ore textures for all deposits are similar with some slight variations (e.g. presence of uranium minerals). This suggests the genetic processes are similar (e.g. Kissin, 1992; Staude et al., 2012). Kissin (1992) suggests mafic rocks are a source for cobalt and nickel; however, mafic rocks only occur near some deposits (e.g. Thunder Bay).

Carbonaceous black shales and their metasedimentary counterparts are also considered a potential source of metals (Burke 2019). Recent models suggest these deposits form as a result of fluid mixing between metalliferous basement brines, basinal marine brines and methane along structures in rift environments and these results in ore deposition (Markl et al., 2016; Burisch et al., 2017). The methane serves as a reductant allowing for the precipitation of sulfides and arsenides (Burisch et al., 2016). Sulfarsenides exhibit compositional zoning from Ni-, to Co, to Fe-rich reflecting an increase in pH during their crystallization, based on the solubilities of analogous Ni-Co-Fe- oxides (Markl et al., 2017). The pH increase coupled with carbon dioxide produced through the oxidation of methane allows for precipitation of calcite gangue late in the paragenesis (Markl et al., 2016).

The element assemblage of the NFDO is also similar to that present in metasediment hosted Co-Cu-Au deposits (e.g. Skuterud Deposit, Norway; Blackbird Deposit, British Columbia, Canada). The classification of Co-Cu-Au metasedimentary deposits is based on mineralogical, alteration, and geological features of well known deposits. The deposits consist of disseminated to massive Co-sulfarsenides and sulfides with Fe-and Cu-bearing sulfides and local Au mineralization. These deposits are typically Proterozoic in age, and

hosted in rift associated, siliciclastic metasediments (Slack, 2010). Byproducts of these deposits include but are not limited to, Ag, Bi, Mo, Ni, Pb, and REEs (Slack, 2012). The most well known examples of these deposits are located in the mining districts at Blackbird, Idaho, Skuterud, Norway, and Kouvervarra, Russia (Slack, 2010). The metal grades of these deposits are variable. The metal grades of these deposits are variable and the orebodies are surrounded by alteration zones consisting of biotite, quartz, albite, and garnet (Slack, 2012).

The majority of the deposits and districts are hosted in metasedimentary rocks of deformed Proterozoic intracontinental basins (e.g. Blackbird and Modum districts). Host rock protoliths are shallow-water marine sedimentary rocks (Slack, 2010). Dehydration of the metasediments during regional metamorphism leads to the generation of metal-rich fluids that precipitate metals in sulfide- and sulfarsenide-rich lenses, veins and breccias.

Regional Geology

The NFDO is hosted in the Meguma Terrane of southern Nova Scotia, which represents the most eastern exposed terrane of the Appalachian Orogen in the Atlantic Provinces of Canada (**Figure 1**). The Meguma Terrane comprises metasedimentary rocks of the Cambrian to Ordovician Meguma Supergroup, metasedimentary and metavolcanic rocks of the Ordovician to Devonian Rockville Notch Group, as well as associated mafic intrusions and numerous granitic plutons of the Devonian-Carboniferous South Mountain Batholith (SMB). The sedimentary and volcanic rocks of the Meguma Terrane accreted onto Laurentia during the Devonian Acadian Orogeny and, in the Annapolis Valley area, experienced predominantly greenschist facies metamorphism prior to the emplacement of the SMB (Shellnut et al., 2019).

The Rockville Notch Group is of interest to this study as it contains the Kentville Formation, host rocks to the NFDO. The Rockville Notch Group is a succession of i) metavolcanics and interbedded quartzite and slate of the White Rock Formation, which are overlain in turn by ii) marine slates and metasiltstones of the Kentville Formation, iii) marine mudstones, siltstone, sandstone, and limestone of the Torbrook Formation, and iv) metasedimentary and mafic volcanics of the New Canaan Formation (White et al., 2017).

The Meguma Supergroup and Rockville Notch Group were intruded by the late Devonian (380 to 365 Ma), syn- to post-tectonic granitic plutons of the SMB (McKenzie and Clarke, 1975), which was likely derived from partial melting of granulite facies Avalonia basement rocks below the Meguma Terrane (e.g., Shellnut et al. 2015). Of importance to this study is the Cloud Lake Pluton of the SMB that intrudes the Kentville Formation and outcrops near the NFDO (MacDonald and Clarke, 2017). Two generations of mafic sills also intrude the Meguma Supergroup metasediments: i) Neoproterozoic to early Ordovician Type 1 mafic intrusives crosscut the Halifax Group of the Meguma Supergroup, and ii) early to middle Devonian, Type II mafic sills crosscut the Halifax Group and White Rock, and Torbrook formations (e.g. Barr et al., 2003; Barr et al., 1983).

The Meguma Terrane uncomfortably underlies the late Devonian to Carboniferous Maritimes Basin (148,000 km^2), which was deposited after rapid uplift and exhumation of the Meguma (Gibling, 2008). The basin reached a maximum thickness of 12 km and comprises mid-Devonian to Carboniferous-aged sedimentary rocks, including the basal alluvial to fluvial conglomerates of the upper Devonian to Carboniferous Horton Group, and the unconformably overlying marine evaporites of the Mississippian Windsor Group.

The Maritimes Basin is not preserved at NFDO; however, rocks of the Windsor Group are located in Windsor, Nova Scotia.

Field Relationships and Sampling

Field mapping and sampling was carried out to show the location of the major lithologies and crosscutting relationships observed in the study area (**Figure 3**; **Table 1**). In the study area, the metasediments are dark-grey interbedded slates and metasiltstones that are locally weathered dark brown-red, and exhibit a steeply dipping, slatey cleavage striking 060°/75° (**Figure 4D**). The metasediments are locally intruded by an irregular gabbro intrusion, as well as at least three diabase sills (**Figure 4A**). The metasediments at the south end of the spillway section are intruded by monzogranite of the Cloud Lake Pluton of the SMB as well as several associated felsic dykes. Mafic rocks outcrop in the central portion of the spillway (diabase sills), and at its upstream end near the Womboldt Falls (gabbro). At the top of the falls the gabbro is crosscut by a felsic dyke. The gabbro is dark grey-black and phaneritic (medium-grained) comprising predominately euhedral, lath-like plagioclase and anhedral clinopyroxene with secondary amphibole alteration (sample GB-1; **Figure 4B**).
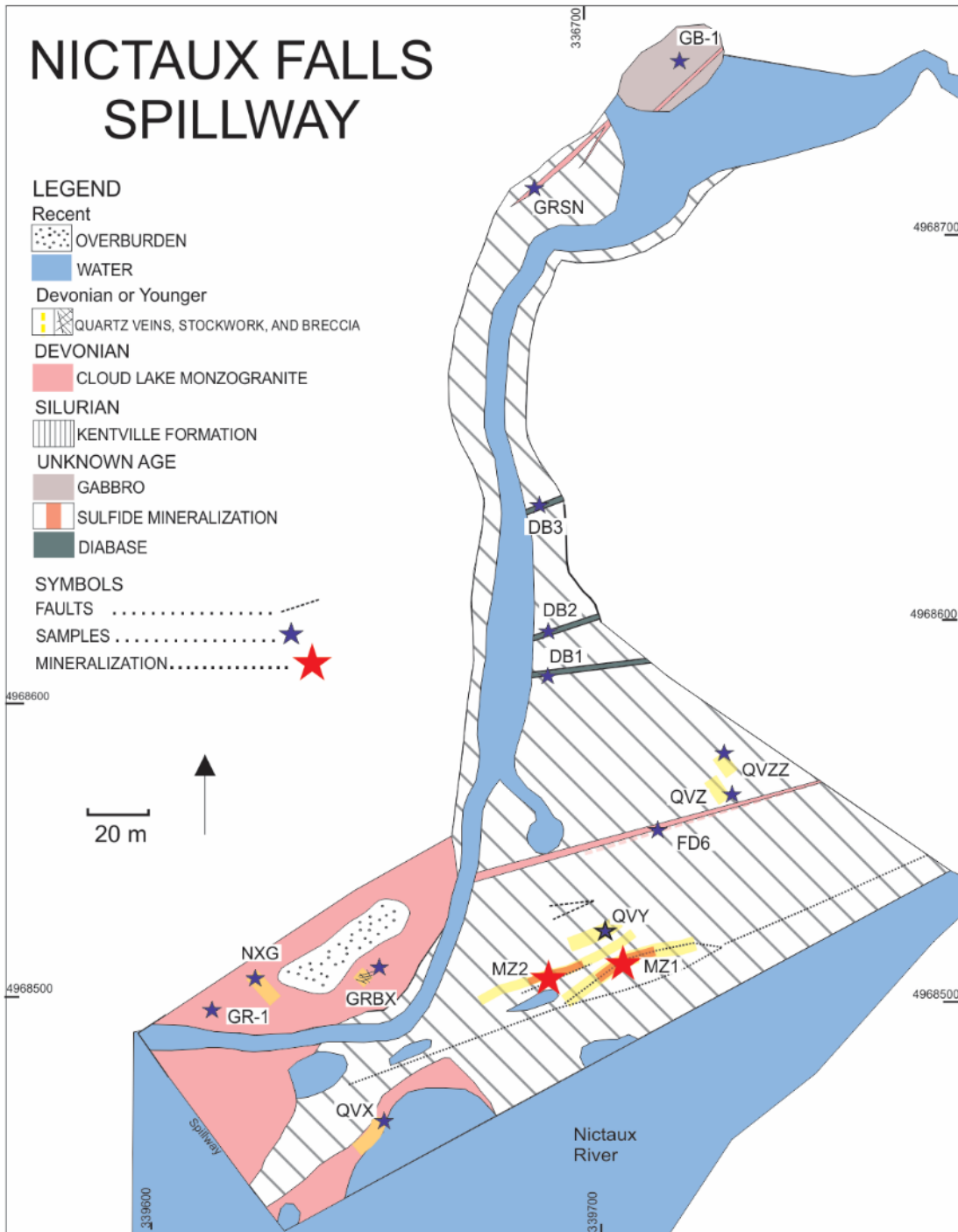
Figure 3: Field map representing the major lithologies and both barren and mineralized quartz veins of the NFDO in the Nictaux Falls Spillway, the Annapolis Valley, Nova Scotia.
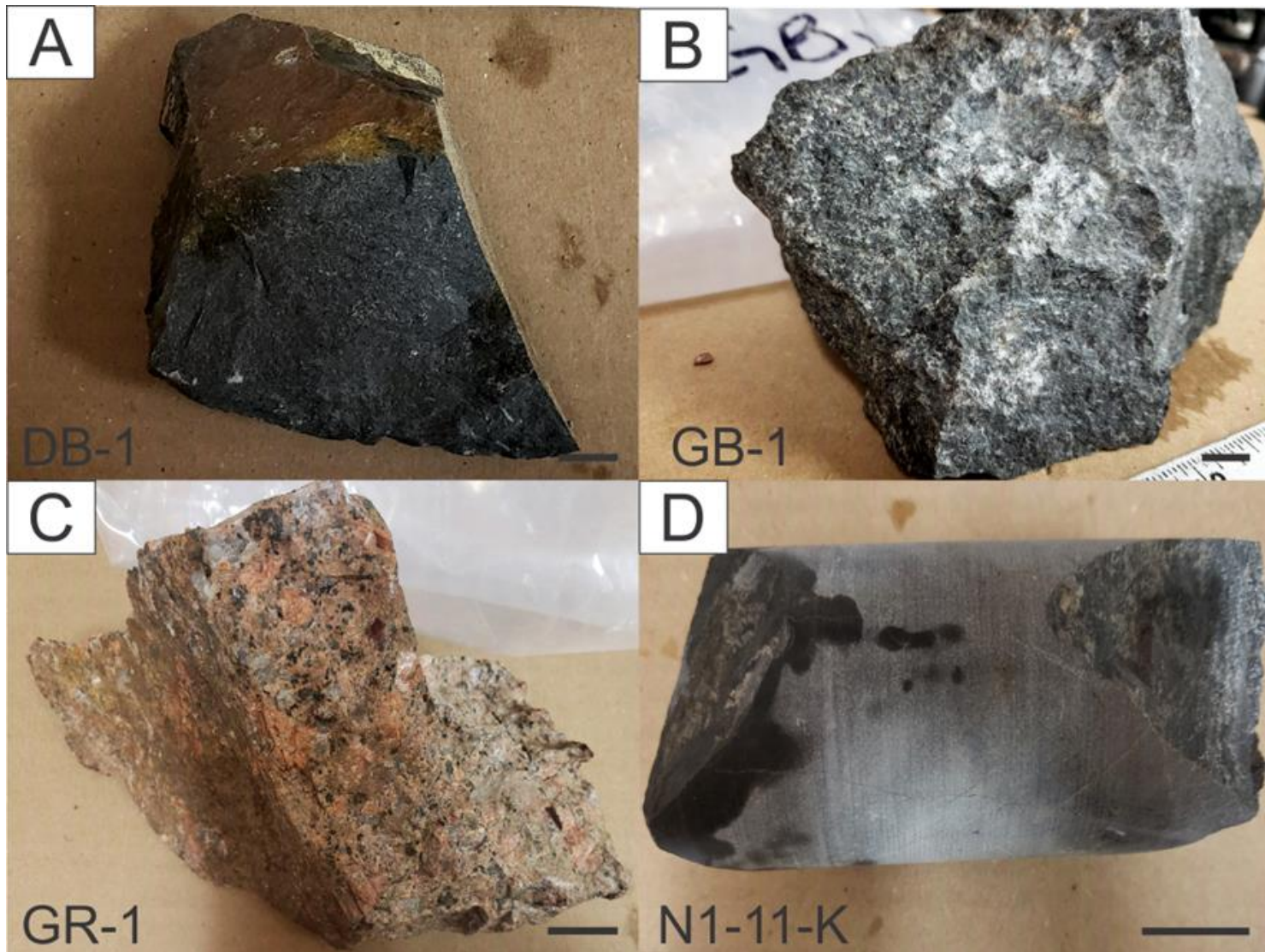
Figure 4: Images of representative samples of the A) diabase (DB-1), B) gabbro (GB-1), C) altered monzogranite (GR-1), and D) unaltered metasediment (N1-11-K). Scale bars are 1 cm.

The relative age of the diabase sills is unknown other than they intrude the Kentville Formation. Crosscutting relationships with other intrusions were not observed. The weathered diabase sills are dark grey-black and aphanitic with late sulfide veinlets (samples DB-1 to 3; **Figure 4A**). The metasediments adjacent to the diabase sills were hornfelsed during contact metamorphism and the contact aureole rocks are grey-blue in colour. The metamorphism overprints the regional slatey cleavage (sample DBHF; **Figure 5B**).

The monzogranite is an irregular shaped intrusion exposed at the southern end of the spillway. It is generally coarse-grained and megacrystic containing cm-scale euhedral feldspar megacrysts in a medium- to coarse-grained groundmass of quartz, plagioclase and biotite (**Figure 4C**), and at surface is weathered reddish-pink. The associated felsic dykes are mineralogically similar to the monzogranite, although they are finer grained and contain lesser biotite (e.g., sample GDY-2). A small (< 20 cm) exposed portion of an approximately 2 m wide felsic dyke near the gabbro outcrop is weathered reddish brown (sample GRSN; **Figure 3C**) indicating the oxidization of sulfide, likely correlating with the greisen that was mapped and sampled in this area by O-Reilly (1995; **Figure 2**). Narrow dykes (< 30 cm wide) are relatively fine-grained or aplitic (samples GDY-1 and FD6). A chilled margin occurs within the monzogranite at its contact with the metasediments. This resulted from chilling of the monzogranite magma against the lower temperature metasediments at the time of its emplacement.

An approximately 150m long, steeply dipping fault-shear zone, striking 263° Az, crosscuts the metasediments. Fault gouge and rocks within the structure are black-grey, relative to the rusty brown weathered metasedimentary wall rock. Evidence for both ductile and brittle deformation is present in the fault-shear zone. In the northwestern portion of the

structure, the metasediments show decimeter scale, asymmetric folds and weak mylonization **(Figure 5E)**. The shear structures indicate right lateral movement. In the southeast portion of the fault-shear zone, the structure branches off into two subparallel segments and the northern segment contains mineralized quartz breccia and stockwork **(Figure 5C, D, H)**. An exposed fault plane in this portion of the structure was used to measure the orientation of the structure **(Figure 5D)**. This smaller fault occurs 8 meters north of the main fault-shear zone. Visible quartz veins (2 cm to 5 cm in width) are exposed on the margins of this fault.

The crosscutting relationships between the fault zone and the monzogranite are somewhat ambiguous. The most southeastern portion of the fault zone diffusely disappears near its contact with the monzogranite, although, it appears that the granite overprints the fault zone. However, the fault crosscuts a felsic dyke in the central portion of the structure **(Figure 5F)**. No crosscutting relationships were observed between the fault and the mafic intrusions.

Numerous hydrothermal quartz veins are exposed in the area within both the metasediments and monzogranite. As previously mentioned, mineralization was observed in the southeastern portion of the fault zone, where the structure dilates and branches. The northern branch of the fault in this area is hereon referred to as the Main Zone. Main Zone 1 samples (labelled MZ1) are the main mineralized quartz stockwork and breccia zone **(Figure 5)**. Sulfarsenide mineralization within MZ1 is silver-grey and fine-grained, occurring in 2 cm wide, early, quartz veins with wall rock laminations. These early veins are crosscut by multiple generations of milky-grey to buff coloured quartz veins, breccia, and stockwork, many of which exhibit coxcomb texture and miarolitic cavities. Four

mineralized samples were collected in this area, in order to represent the mineralization and later quartz (i.e. MZ1-1, MZ1-L, MZ1-LBX, MZ1-BX; **Figure 6**). Main Zone 2 (sample MZ2-1; **Figure 7**) refers to an approximately 5 cm wide mineralized quartz breccia vein that occurs along the exposed fault plane a few meters north of Main Zone 1 (**Figure 3, Figure 5D**). Mineralization in MZ2 occurs in sulfarsenide mineralized wallrock clasts within the quartz breccia. It is clear the sulfarsenide mineralization in the Main Zone is constrained to wall rock material and no subsequent mineralization occurred in the late quartz.

The monzogranite in the western portion of the spillway is crosscut by barren quartz veins (e.g., NXG-1, GRBX), breccia and stockwork, which appear similar to the late quartz in the Main Zone. The veins contain milky-grey quartz and strike opposite of the previously observed veins in the spillway. Similar veins were observed in the monzogranite at the southern portion of the spillway (QVX). The textural similarities between the barren quartz veins and stockwork in both the metasediments and granite suggest a similar timing and origin, after emplacement and crystallization of the monzogranite. The monzogranite proximal to the quartz veins is altered by a disseminated biotite and deep red staining of K-feldspar (sample GR-1;**Figure 4C**), suggesting possible potassic alteration.
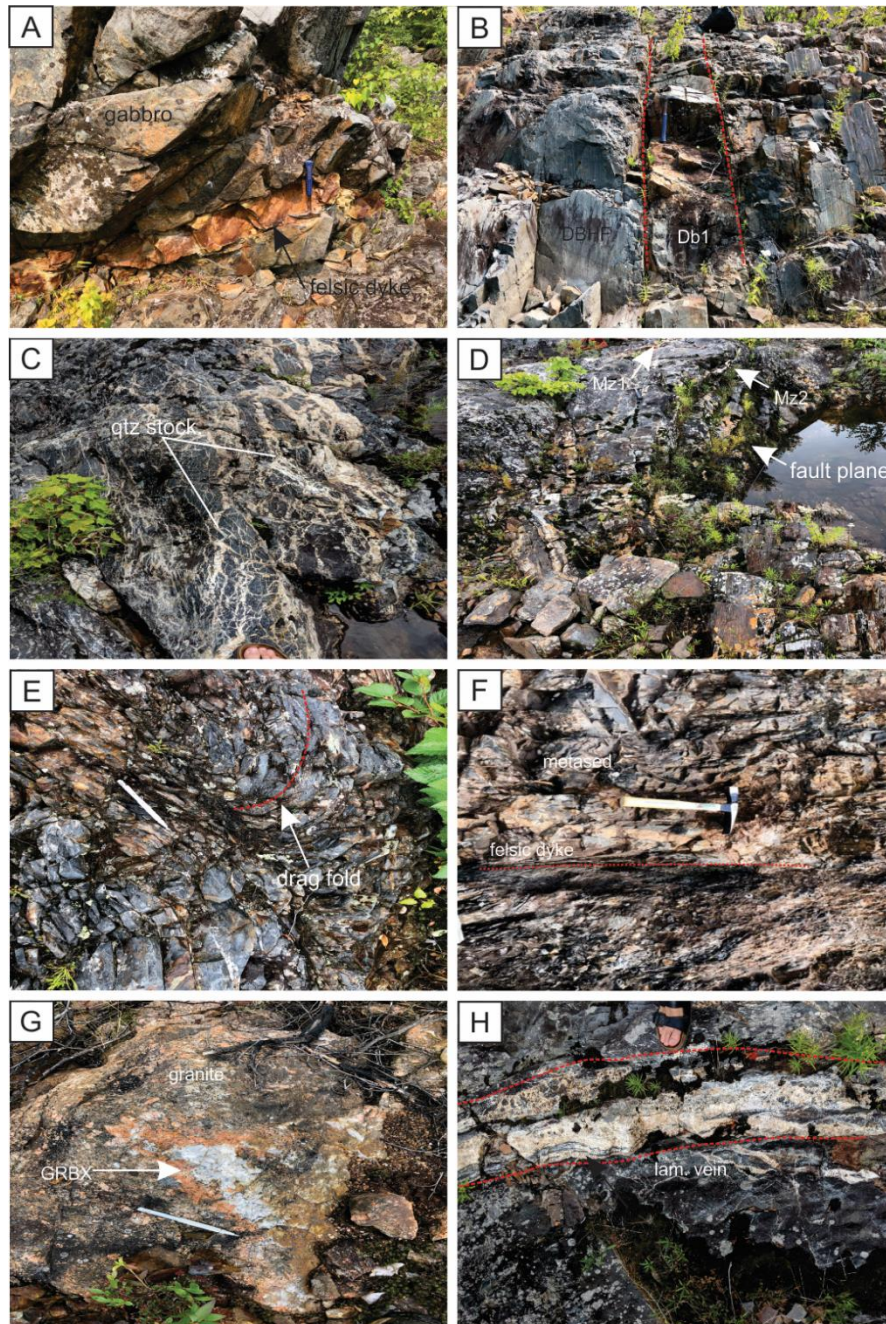
Figure 5: Images showing the crosscutting relationships and occurrence of quartz veins hosted in the NFDO in the Annapolis Valley, Nova A) A felsic dyke crosscuts the gabbro. B) A diabase sill (DB-1) crosscuts the metasediment. The rocks on either side of the dyke are hornfelsed (DBHF). C) Quartz stockwork in the metasediment in Main Zone 1. D) An exposed fault plane in Maine Zone 2 (MZ2). Main Zone 1 is shown in the upper left (MZ1). E) Weak mylonization of the metasediments in the fault-shear structure. F) A felsic dyke crosscut by faulting. G) Granite hosted barren quartz breccia. H) Fault bound MZ1.

Table 1: Locations and descriptions of sampled lithogies and veins of the NFDO in the Nictaux Falls Spillway, the Annapolis Valley, Nova Scotia (UTM Zone 20N NAD 83)

Sample	Easting	Northing	Sample Description
GB-1	339703	4968727	Gabbro containing heavy amphibole altering with detectable quantities of Co and Ni.
DB-1	339697	4968585	Diabase sill containing heavy amphibole altering with detectable quantities of Co and Ni.
DB-2	339689	4968594	Diabase sill containing heavy amphibole altering with detectable quantities of Co and Ni.
DB-3	339684	4968623	Diabase sill containing heavy amphibole altering with detectable quantities of Co and Ni.
QVZ	339723	4968558	Quartz vein sample containing no sulfarsenide mineralization.
QVY	339691	4968518	Quartz vein sample containing no sulfarsenide mineralization.
MZ2-1	339673	4968513	Quartz vein from main zone 2
GRBX	339644	4968508	Sample of granite breccia containing no sulfarsenide mineralization
GR-1	339619	4968501	Cloud Lake monzogranite containing small concentrations of arsenopyrite
FD6	339747	4968558	Felsic dyke sample mineralogically similar to granite.
QVX	339647	4968471	Quartz vein sample containing no sulfarsenide mineralization.
MZ1-La	339687	4968511	Quartz vein sample from main zone 1 section a containing sulfarsenides and late quartz generations.
MZ1-Lb	339687	4968511	Quartz vein sample from main zone 1 section b containing a sulfarsenide veinlet surrounded by late quartz generations
MZ1-LBX	339687	4968511	Quartz vein sample from main zone 1 containing late brecciated and laminated quartz.
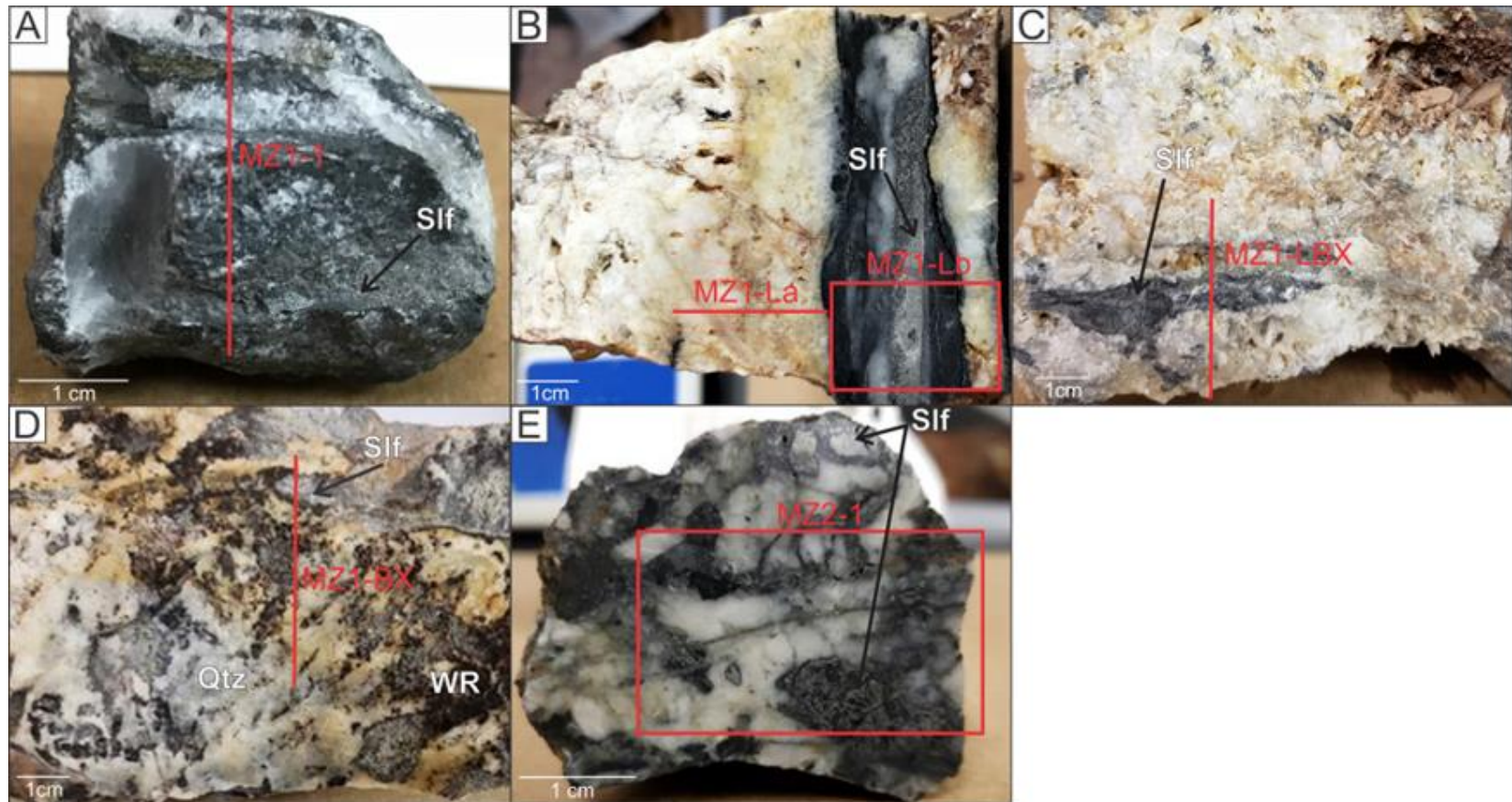
Figure 6: Photographs of mineralized samples A) MZ1-1, B) MZ1-L, C) MZ1-LBX, D) MZ1-BX, and E) MZ2-1.
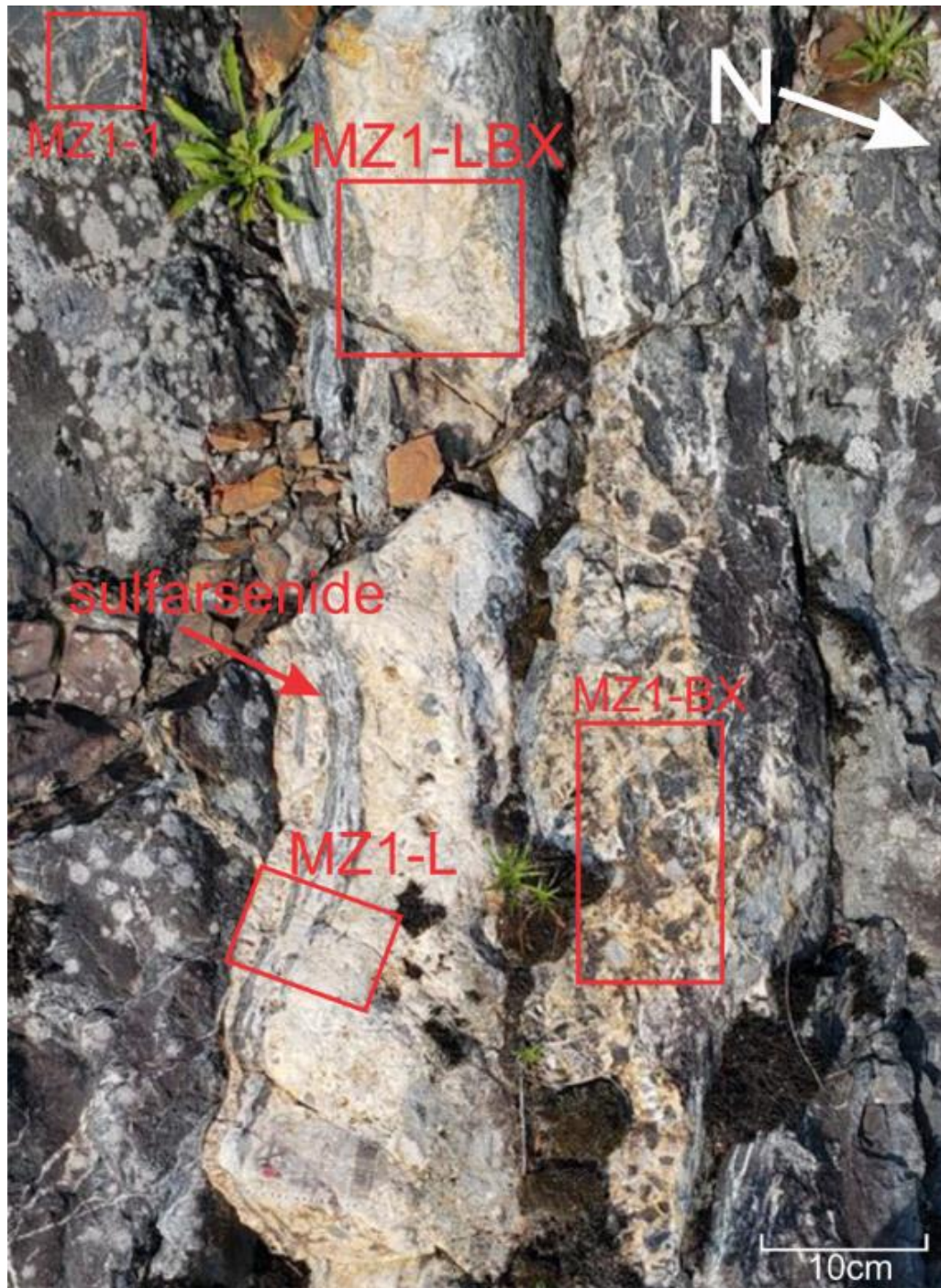
Figure 7: A photograph of mineralized quartz breccia and stockwork of Main Zone 1. Samples collected are indicated in red.

Analytical Methods

Petrography

Samples were first examined in hand specimen for major minerals and textures and were then cut into blocks and sent to Vancouver Petrographics Ltd. for polished thin section preparation. Detailed petrographic analysis was completed on the polished thin sections under plain polarized light and crossed polarized light with the use of transmitted and reflected light microscopy. The thin sections were then carbon coated and analysed by a TESCAN MIRA 3 LMU Variable Pressure Schottky Field Emission Scanning Electron Microscope (SEM; Saint Mary's University) in order to better examine the textures and relationships between individual minerals using back-scattered electron (BSE) imaging, and identify unknown mineral phases. Semi-quantitative mineral compositions were obtained with an energy-dispersive spectroscopy (EDS) detector using an acquisition time of 30 seconds, accelerating voltage of 20kV, and a working distance of 17mm. The data were resolved using the INCA software.

Electron Probe Microanalyzer

Four representative mineralized samples (MZ1-1, MZ1-Lb, MZ1-LBX, MZ2-1) were chosen for EPMA analysis of sulfarsenides. Compositional data for the sulfarsenides was obtained, for 62 data points, in order to quantify and localize the elemental distributions of major components in the sulfarsenides. Quantitative analyses were completed by an electron probe micro-analyzer using a JEOL JXA8230 5-WDS instrument at the University of Toronto. Samples were sent to Toronto and spot analyses and mapping was completed at Saint Mary's University in Halifax, Nova Scotia using a computer program called TeamViewer which allowed for the operation of the EPMA at Saint Mary's University.

Operation conditions were 20kV at a beam current of 20nA, with peak counting times of 60 s and a peak background of 10 s. Standards used are as followed: synthetic arsenopyrite (Fe-As-S), Co metal (Co), natural pentlandite (Ni), $Au_{80}Ag_{20}$ (Au), $FeTe_2$ (Te), $AgBiS_2$ (Ag-Bi), and CuSbS (Sb).

Micro-XRF

Six representative samples (GB-1, DB-1, DB-2, DB-3, MZ1-Lb, MZ1-LBX) were chosen for elemental mapping using Micro-XRF. Mapping was completed in order to map the distribution of Fe, Co, and Ni in the mafic intrusions and the sulfarsenides. Samples were sent to the University of New Brunswick and mapped using a Bruker M4 Tornado instrument, mapping the distribution of elements within the polished thin sections. Operation condition consisted of a beam diameter of 20µm and measurements every 20µm, with a tube power with 400 mA and 50 W.

S-isotopes

Isotopic analysis for $^{34}S/^{32}S$ of bulk sulfarsenide from both Main Zones (samples MZ1-Lb, MZ1-LBX, MZ2-1) were measured using a Delta Plus ZP isotope ratio mass spectrometer at the Jan Veizer Isotope Laboratory at the University of Ottawa using the following analytical procedures. Approximately, 0.4 mg of sample was weighed and put into tin capsules with a minimum of 0.8 mg of tungstic oxide. The samples were then put into the isotope cube elemental analyzer at 1800°C to be flash combusted and devolatilized. Helium was used to transport the gases through the elemental analyzer to be cleaned and separated. Gaseous SO_2^- is transported to the mass spectrometer by a conflo IV interface in order to detect and determine S^{34}/S^{32} ratios. The values are reported as ‰ $\delta^{34}S$ relative to the Vienna Canyon Diablo Troilite standard using the following equation:

$$\delta^{34}S = \left(\frac{\left(^{34}S/^{32}S\right)_{sample} - \left(^{34}S/^{32}S\right)_{reference}}{\left(^{34}S/^{32}S\right)_{reference}} \right) \times 1000$$

.Based on measurements of the standard, Vienna Canyon Diablo Troilite, the analytical precision is estimated at ± 0.2 ‰

Whole Rock Geochemistry

The bulk geochemistry of the mineralized and unmineralized samples was determined at Geolabs in Sudbury, Ontario. Samples were prepared by cutting and weighing approximately 100 g of each sample for major, minor, and trace elements quantification. For host lithologies, major and minor elements were determined via X-ray fluorescence. Samples were prepared as glass beads for analysis using a borate flux to fuse calcined samples. Loss on ignition was measured in two increments: the sample was heated to 105°C under nitrogen atmosphere in order to release any pore volatiles, and 1000°C under oxygen atmosphere to release structurally bound volatiles. The results are expressed as weight% oxide, and were renormalized to exclude volatiles. Trace elements were determined using inductively coupled plasma mass spectrometry (ICP-MS) after preparation by aqua regia extraction.

The composition of mineralized samples (MZ1-Lb and MZ2-1) was quantified by inductively coupled plasma atomic emission spectroscopy (ICP-AES) using open vessel digestion techniques. Measurements for Co, Cu, and Ni were determined using flame atomic absorption analysis.

Results

Petrography

Petrographic studies were completed for all lithologies and veins collected at the NFDO. Emphasis is placed on mineralized quartz veins, as well as mafic intrusions and

metasediments due to their potential to source metals. The petrographic reports for the remaining samples are shown in **Appendix Petrography 1** and **Appendix Petrography 2**. The SEM analyses for all of the samples are located in **Appendix Table 1** to **Appendix Table 17**.

Mineralized Quartz Veins
Mineralized quartz veins from the Main Zone 1 (samples MZ1-Lb, MZ1-1, MZ1-LBX) consist predominantly of sulfarsenide and quartz with chlorite and sericite-rich wall rock laminations **(Figure 8A)**. The veins are heterogeneous, with sulfarsenides occurring as clusters of blocky euhedral grains and euhedral quartz on the other **(Figure 6)**. Compositional zoning is observed with BSE imaging where euhedral Fe-rich cores transition to broad Fe- and Co-rich zones to relatively fine Ni-rich rims **(Figure 8B)**. Rounded pyrite grains, sometimes containing inclusions of galena, occurs as inclusions within the sulfarsenides **(Figure 8C,E)**. The sulfarsenides in contact with pyrite inclusions contains high Ni (up to 16 wt%). Rutile occurs interstitial to sulfarsenide minerals with chlorite, sericite and an unidentified, very fine-grained REE-rich silicate **(Figure 8D,F)**. This assemblage was likely inherited from the wall rock metasediments due to mineralogical similarities between the interstitial mineral phases of the Main Zones and the Kentville Formation sample. The rutile occurs in equilibrium with sulfarsenide and quartz; however, the chlorite shows a reaction rim with quartz, suggesting that the quartz is late with respect to mineralization and the wall rock. The mineralized veins are locally crosscut by later quartz veins and breccia. Later quartz exhibits coxcomb texture. The major mineral assemblage is consistent for all veins located in MZ1.
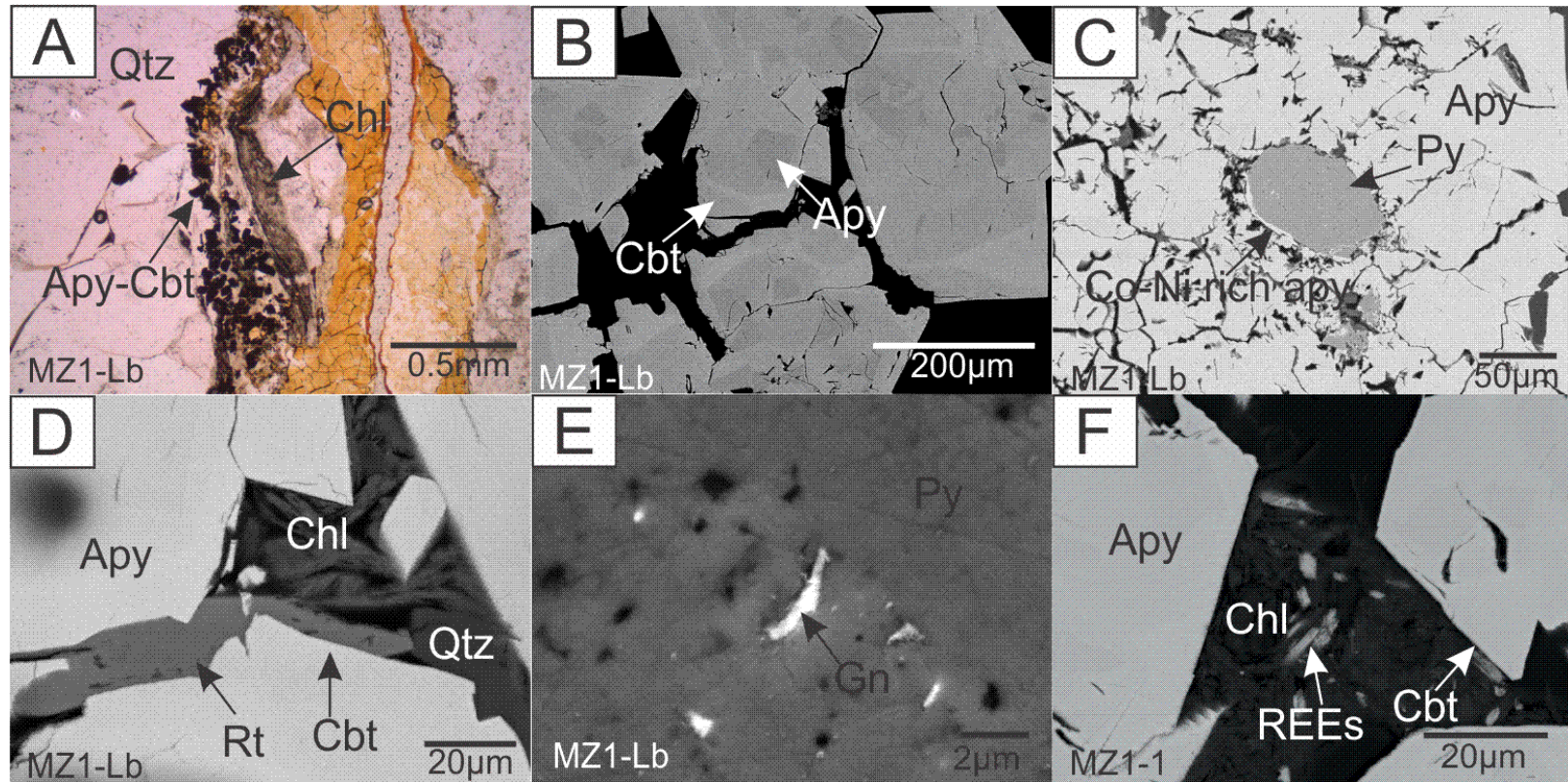
Figure 8: Representative images of mineralized veins in Main Zone 1. A) A photomicrograph of the chlorite-bearing wall rock lamination hosting primary sulfarsenide mineralization (opaques) in sample MZ1-Lb. B) A BSE image of zoned sulfarsenide showing euhedral arsenopyrite cores that transition to cobaltite-rich rims in sample MZ1-Lb. C) A BSE image of early Ni-rich pyrite surrounded by sulfarsenide mineralization in sample MZ1-Lb. The rim of the sulfarsenide is close to gersdorffite in composition. D) A BSE image of rutile in equilibrium with surrounding sulfarsenide, quartz and chlorite in sample MX-Lb. E) A BSE image of galena inclusions in Ni-rich pyrite in sample MZ1-Lb. F) A BSE image of interstitial chlorite surrounded by cobaltite-arsenopyrite grains, hosting very fine-grained REE-rich silicates in sample MZ1-1.

Mineralization from Main Zone 2 (sample MZ2-1) is characterized by sulfarsenide-mineralized metasediment clasts in quartz breccia. The sulfarsenide mineralization exhibits net texture and is constrained to chloritized wall rock clasts and not in the late quartz **(Figure 6E)**. Sulfarsenide mineralization is similar to MZ1, as it occurs with wall rock material, is compositionally zoned, and surrounded by later quartz **(Figure 9A,B)**. Additionally, Au-Ag alloy occurs interstitial to the Ni-rich rims (**Figure 10A-D**). Accessory mineral phases in MZ2 are similar to accessary mineral phases in MZ1 (i.e. rutile and pyrite; **Figure 9C**).
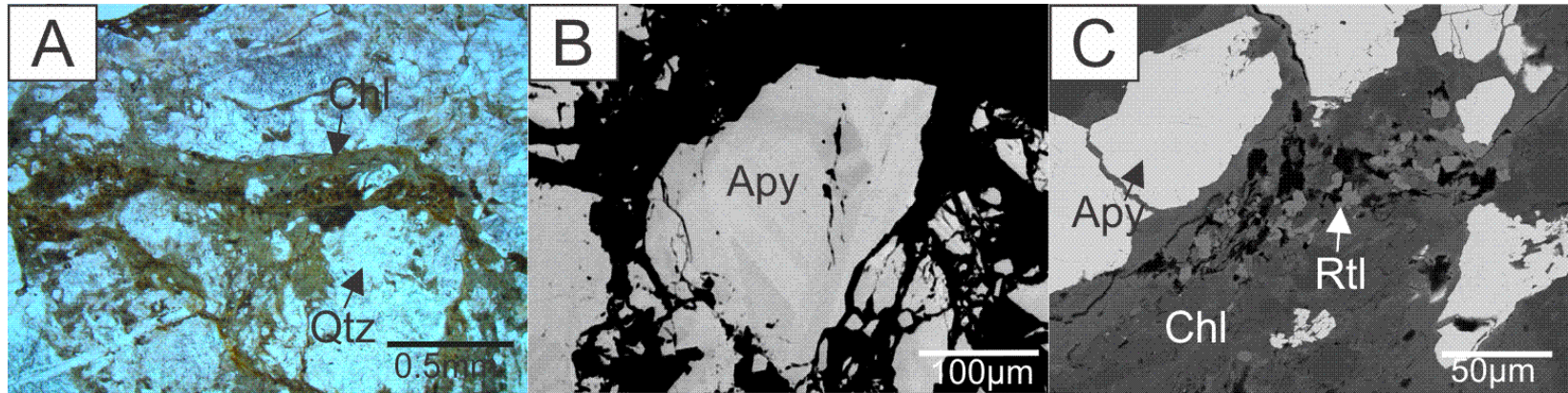
Figure 9: Representative images of mineralization in sample MZ2-1 A) Photomicrograph of chloritized wall rock clasts surrounded by later euhedral quartz in sample MZ2-1. B) A BSE image of zoned sulfarsenide showing transitioning between arsenopyrite and cobaltite-gersdorffite in sample MZ2-1. C) A BSE of secondary anhedral rutile surrounded by arsenopyrite-cobaltite grains in sample MZ2-1.
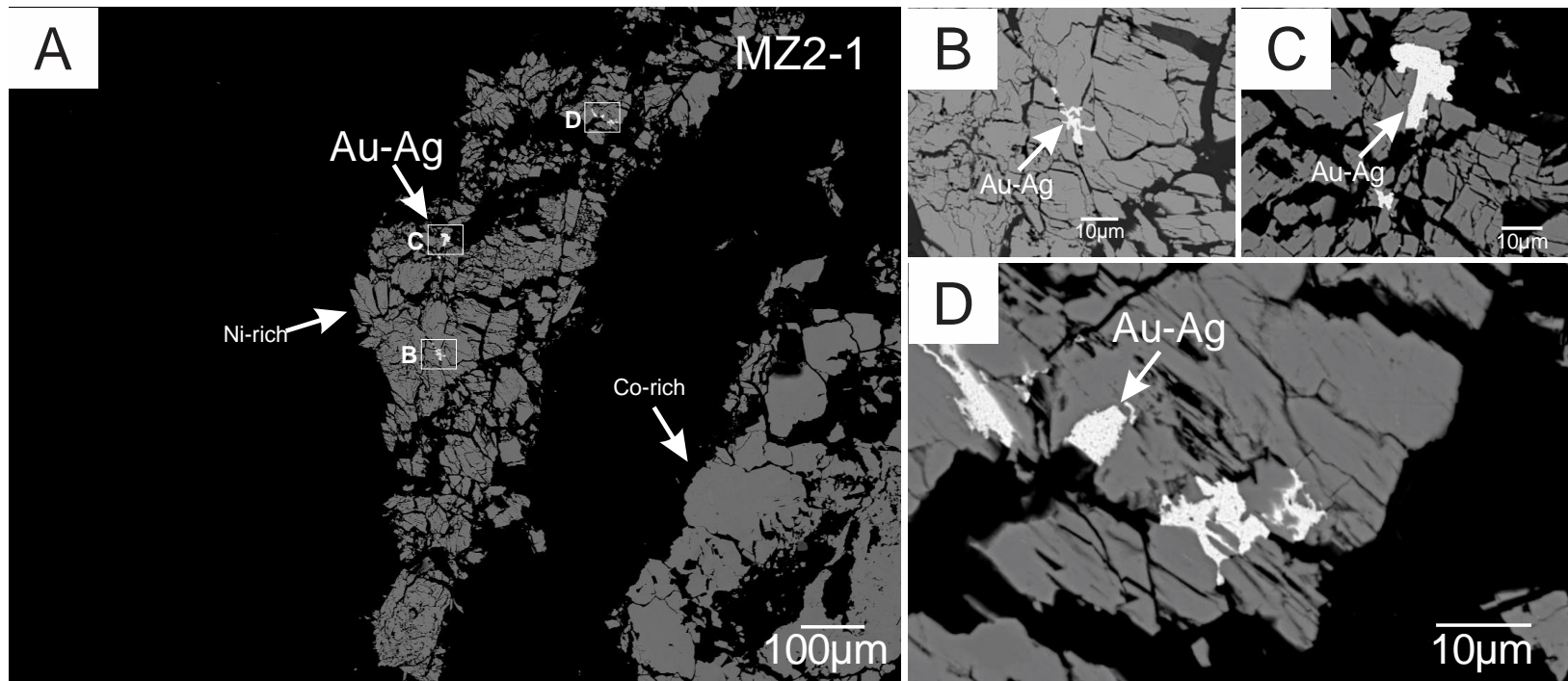
Figure 10: Representative BSE images of the Au-Ag alloy interstitial to Ni-rich sulfarsenides hosted in MZ2 in Nictaux Falls, Annapolis Valley, Nova Scotia

Unmineralized Rocks

The following petrographic descriptions characterize the representative samples of the Kentville Formation and the mafic intrusions associated with the NFDO to consider these rocks as potential metal sources. Petrographic observations of the remaining unmineralized samples are tabulated in the **Appendix Petrography** section.

The Kentville Formation metapelite (sample KF-1) is characterized by primary Ti-rich biotite (30 modal%), Fe-Mg chlorite (35%), quartz (35%), ilmenite (<1 %), and Ni-rich pyrite (<1 %) (Appendix Table 1; **Fig. 1A,B**). Biotite is subhedral (50 to 75 µm in size) and weakly-moderately foliated with local porphyroblasts (up to 250 µm; **Figure 11A**). Anhedral quartz (50 to 100 µm), subhedral pyrite (20 to 70 µm) and euhedral ilmenite (<10 µm) occur disseminated throughout the rock (**Figure 11B**). Secondary pyrite occurs as stringers, which crosscut the primary mineral assemblage. Pyrite stringers are bordered by K-feldspar **(Figure 11C)**. The Kentville Formation near the margins of diabase sills (sample KF-HF) underwent contact metamorphism. These rocks are fine-grained hornfels (no foliation), with biotite recrystallized to form euhedral laths. The major mineral assemblage of these rocks is similar to that of the protolith; however, the mineralogy of accessory phases is varied. Analysis using SEM identified compositionally intermediate plagioclase, chalcopyrite, titanite, monazite, galena, and REE-silicates **(Figure 11D)**. In addition, chlorite and titanite contain detectable quantities of Co and Ni.
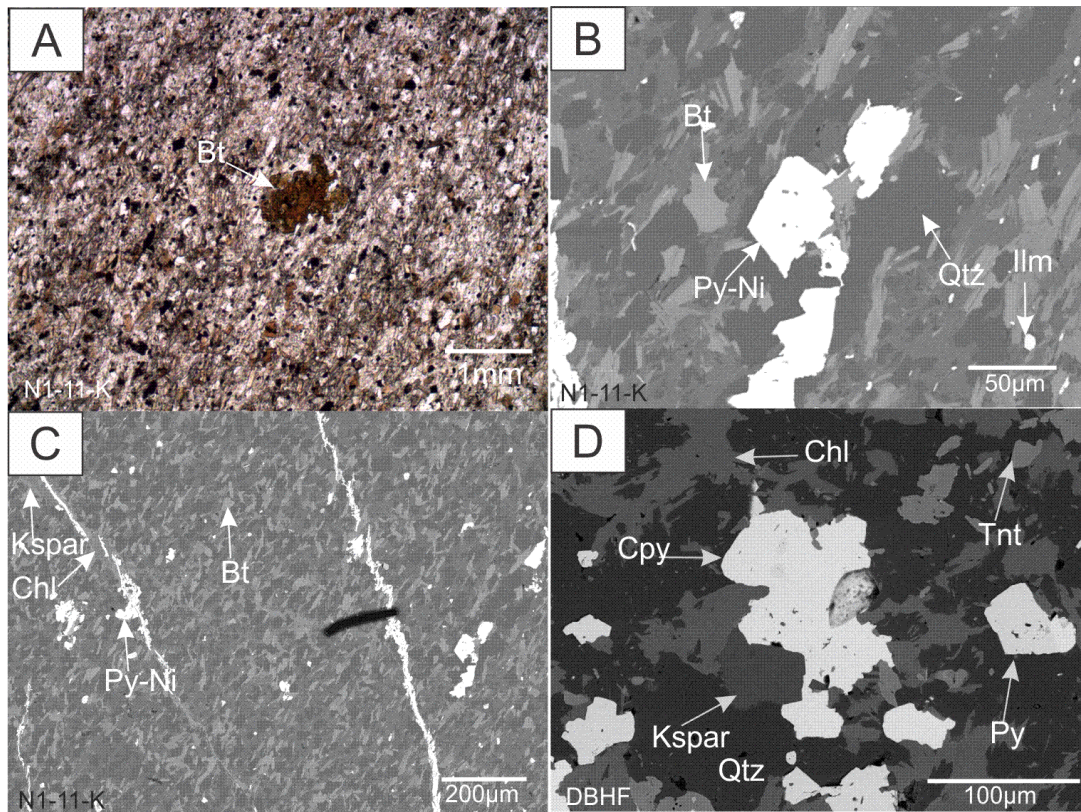
Figure 11: Representative images of samples of the Kentville Formation metasedimentary rocks. A) A photomicrograph of an anhedral biotite (Bt) porphyroblast surrounded by a fine-grained matrix of quartz, biotite and chlorite in sample N-11-1-K. B) A BSE image of primary Ni-rich pyrite (Py) surrounded by biotite, quartz (Qtz) and chlorite (Chl) with disseminated ilmenite (Ilm) of sample N-11-1-K. C) A BSE image showing secondary pyrite stringers with K-feldspar (K-spar) crosscutting the primary mineral assemblage of KF-1. D) A BSE image of anhedral chalcopyrite (Cpy) surrounded by subhedral titanite (Tnt), and blocky pyrite in sample DBHF.

The gabbro (sample GB-1) exhibits pseudo-ophitic texture and is characterized by primary lath-like intermediate plagioclase (3 to 5 mm) partially included by anhedral clinopyroxene (augite), with chlorapatite and ilmenite and accessory to trace cobaltite, titanite, pyrite, zircon, and baddeleyite. Clinopyroxene is anhedral (4 to 5 mm) and largely altered to amphibole (actinolite) **(Figure 12A)** and Fe-rich biotite (3 to 5 mm) **(**Error! Reference source not found.**B)**. Clinopyroxene also exhibits ilmenite exsolution **(Figure 12E)**. Secondary pyrite occurs as disseminated grains sometimes altered to chalcopyrite or Ni-rich pyrite **(Figure 12E,F)**. The diabase sills (DB-1, DB-2, DB-3) are fine-grained, contain relict plagioclase and are pervasively altered by amphibole (actinolite), biotite and lesser chlorite. Analysis using SEM identified chalcopyrite, pyrite, titanite, ilmenite, intermediate plagioclase, allanite, and sphalerite **(Figure 12J, K, and L)**; although, more work is required to constrain their paragenesis. In addition, chlorite and amphibole alteration contain detectible quantities of cobalt (<1 wt%) using EDS.
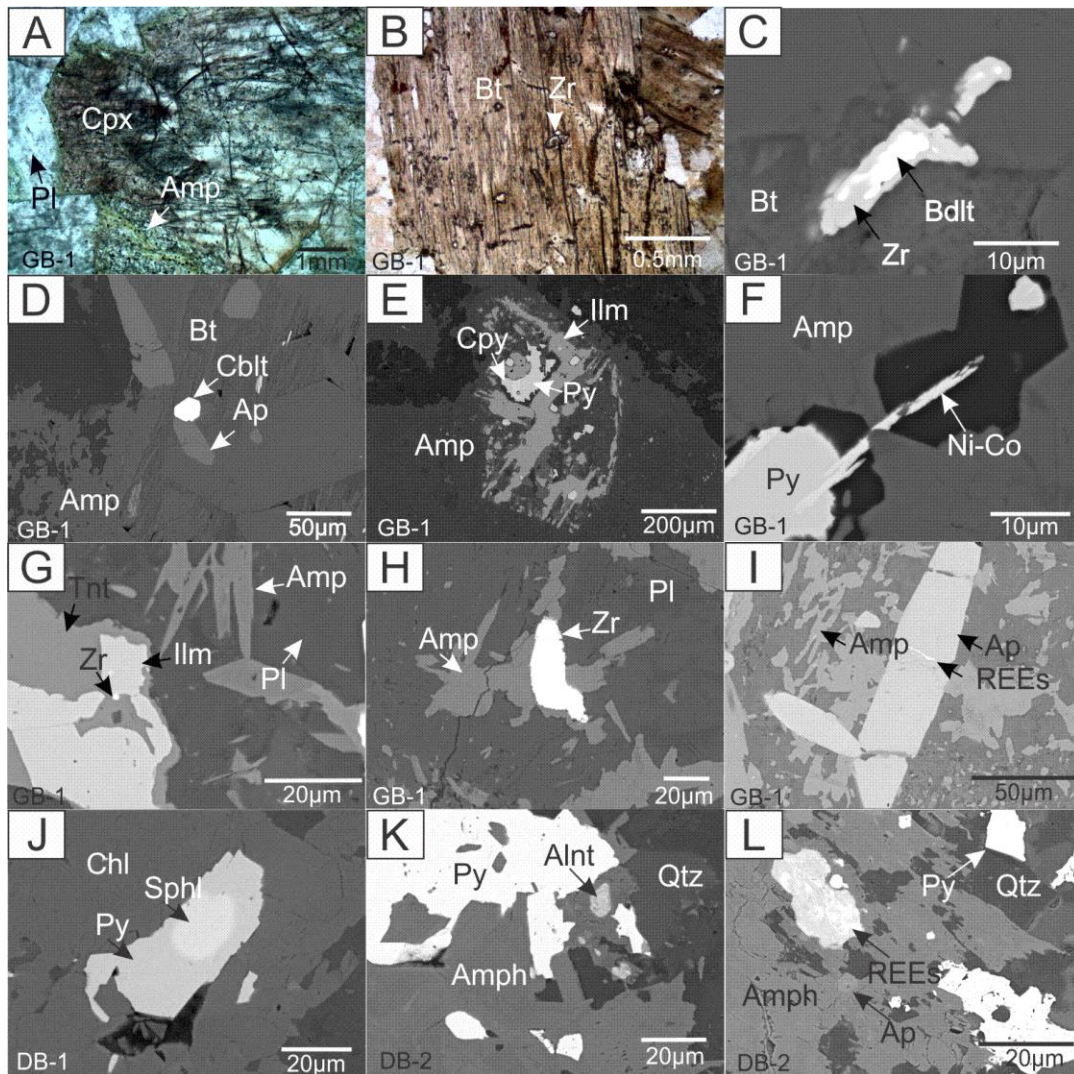
Figure 12: Representative images of the mafic samples. A) A photomicrograph of a large clinopyroxene (Cpx) grain with plagioclase (Pl) altered by amphibole (Amp) in sample GB-1. B) A photomicrograph of secondary biotite (Bt) hosting a euhedral zircon in sample GB-1. C) A BSE image of a relict inclusion of baddeleyite rimmed by zircon in amphibole and fine-grained biotite in sample GB-1. D) A BSE image of primary euhedral cobaltite and apatite surrounded by secondary biotite and amphibole in sample GB-1. E) A BSE image of clinopyroxene altered by amphibole in sample GB-1. Clinopyroxene contains inclusions of pyrite and ilmenite, and also exhibits crystallographically controlled ilmenite exsolution. F) A BSE image of pyrite altering to secondary Ni-Co rich grains surrounded by amphibole alteration in sample GB-1. G) A BSE image of lathlike amphibole hosting inclusions of zircon, titanite, and ilmenite, surrounded by primary plagioclase in sample GB-1. H) A BSE image of secondary amphibole alteration hosting anhedral zircon surrounded by primary plagioclase in sample GB-1. I) A BSE image of secondary apatite hosting REE-rich mineral within fractures, surrounded by amphibole alteration in sample GB-1. J) A BSE image of trace sphalerite rimmed with pyrite, surrounded by chlorite in sample DB-1.

Mineral Chemistry of Sulfarsenides

Elemental Mapping

Selected sulfarsenide grains from mineralized samples were chosen for elemental mapping in order to observe the distribution of major elements. Thin section mapping using micro-XRF **(Figure 13A-D)** shows that the sulfarsenides exhibit unidirectional zoning in the laminated veins and clast style mineralization. The map of the laminated vein shows that arsenopyrite occurs concentrated at the base of the vein, and the proportion of Co (Fe-rich cobaltite) is highest in the middle, with Ni (Co-Fe rich gersdoffite) at the rims where the sulfarsenide is in contact with quartz. Large scale (e.g. 4 mm field of view using 20 μm beam) confirm unidirectional zoning of net-textured sulfarsenide mineralized clasts **(Figure 14)**. These maps as well as fine-scaled (~500 μm field of view using 1 μm beam) WDS-maps **(Figure 13E-G)** indicate early, euhedral arsenopyrite cores of a distinct paragene in the zoned sulfarsenides. These cores are mantled by arsenopyrite, which transitions outwards to Fe-rich cobaltite and Co-Fe rich gersdorffite rims **(Figure 13H-J)**.

Elemental mapping was also carried out on the mafic intrusions due to their potential to source metals **(Figure 15)**.
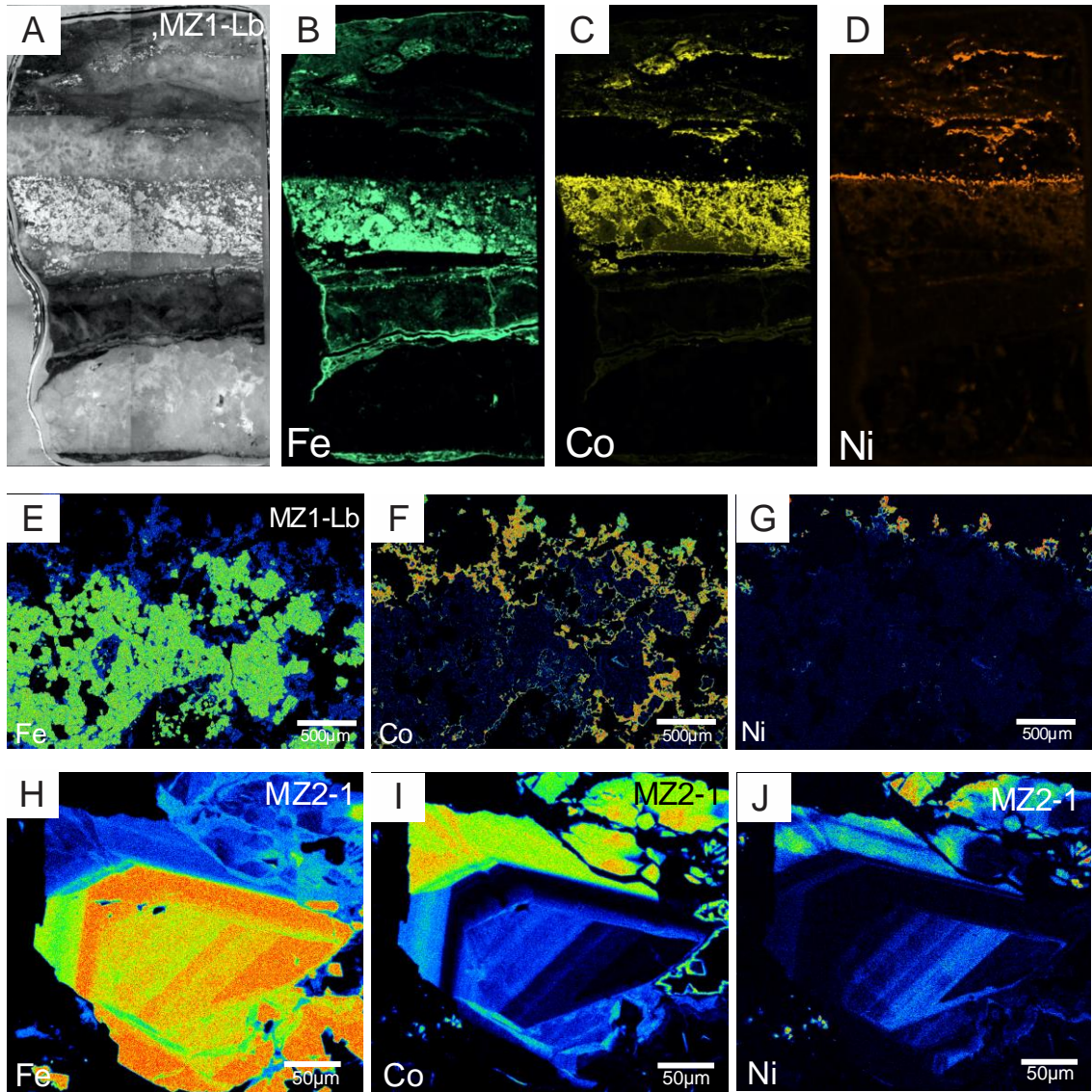
Figure 13: Elemental maps for mineralized veins. (A-D) Thin section mapping completed by Micro-XRF mapping, (E-G) Elemental mapping at 500 µm scale completed by EPMA, (H-J) Elemental mapping on a grain size scale completed by EPMA. Bright colors indicate high concentrations, whereas dark colors indicate low concentrations.
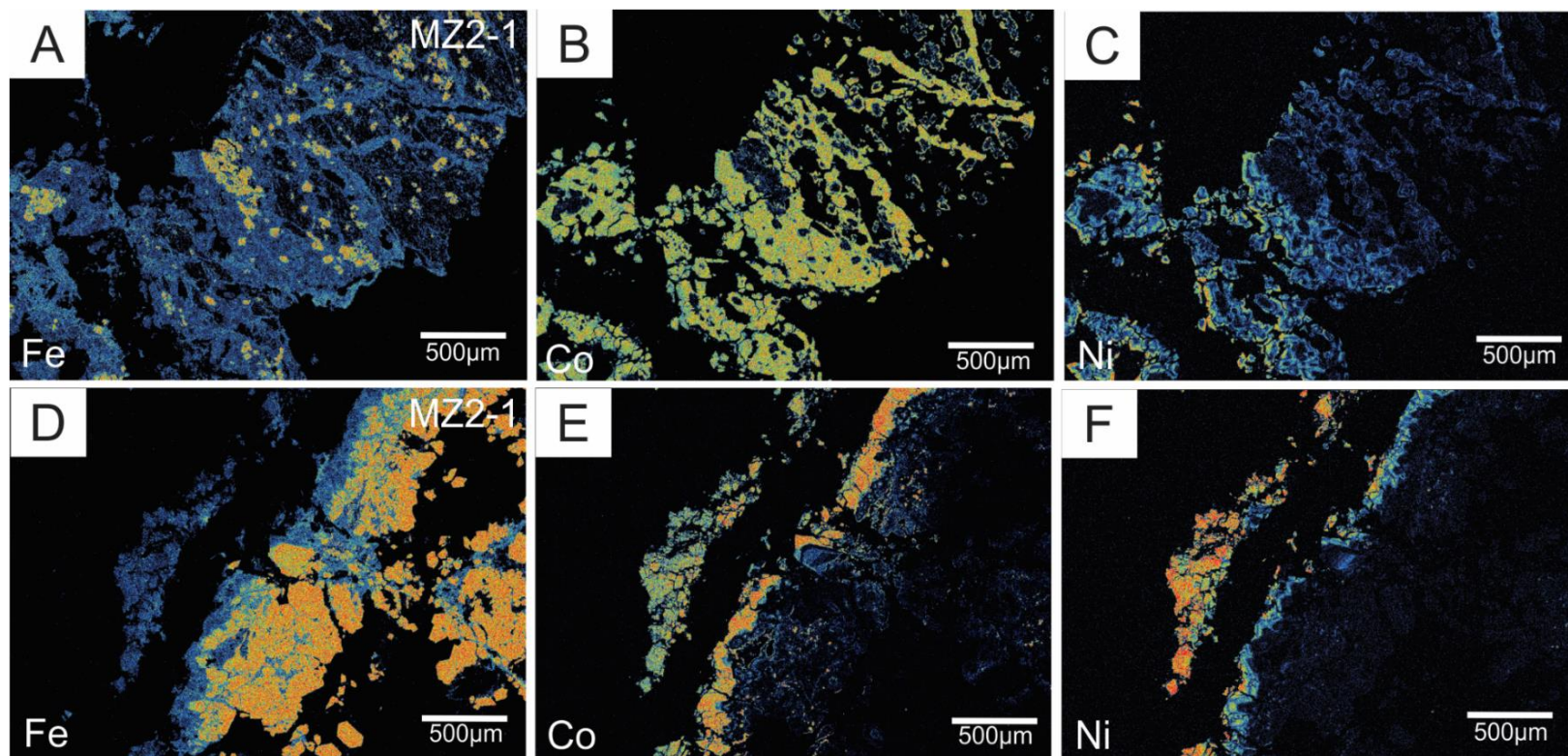
Figure 14: Elemental map of MZ2-1. (A-C) Clast style mineralization exhibiting net texture, and (D-F) Elemental mapping of Fe-Co-Ni rich phases in sample MZ2-1
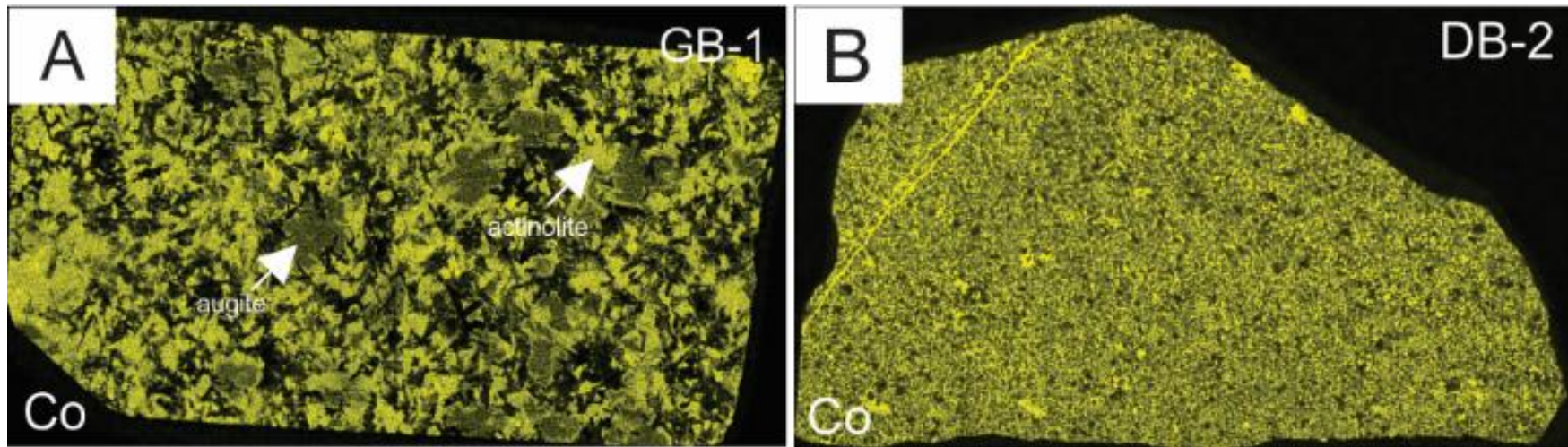
Figure 15: Micro-XRF images of the mafic intrusions (GB-1 and DB-2) sampled from the NFDO. DB-2 is representative of all diabase samples.

Electron Probe Microanalysis

Four representative samples (MZ1-1, MZ1-Lb, MZ1-LBX, MZ2-1) were chosen for EPMA analysis. A total of 62 data points were measured in order to quantify the major and minor elements in the sulfarsenide phases from both MZ1 and MZ2 (representative points are listed in **Table 2,** see **Appendix Table 18**, **Appendix Table 19**, **Appendix Table 20** for entire datasets for each mineral phase). The composition of sulfarsenides do display variation but are similar between the mineralized samples ranging from 0.71 to 35.20 wt.% Fe, Co (up to 33.40), Ni (up to - 10.46), As (39.53 -46.35, S (18.83 – 24.00), and Au (up to – 0.03). Based on these results the sulfarsenides have been classified into the following categories: i) Fe-rich sulfarsenide (arsenopyrite), ii) Co-Fe rich sulfarsenide (Fe-rich cobaltite), and iii) Ni-Co-Fe rich sulfarsenide (Co-Fe-rich gersdorffite) sulfarsenide **(Fig. 16)**. The elemental chemistry of arsenopyrite is quantified by 28 measurements (Error! R eference source not found.). Arsenopyrite contains the highest concentration of Fe (average = 33.51 wt% ± 1.71 wt%, 1σ), with low Co (average = 0.95 wt% ± 1.31 wt%) and Ni (average = 0.20 wt% ± 0.63 wt%). The As (average = 42.47 wt% ± 1.57 wt%) and S (average = 21.8 wt% ± 1.10 wt%) values are exhibit a slight range. The Au content is also variable, ranging from below the detection limit of 0.02 wt% to 1.01 wt% ± 0.01 wt%.

The Fe-rich cobaltite is quantified by 28 measurements (Error! Reference source n ot found.), and is characterized by the highest (although variable) Co content (average = 24.06 wt% ± 7.02 wt%). This phase is slightly less enriched in Fe (average = 11.49 wt% ± 7.28 wt%) relative to the arsenopyrite. Low concentrations of Ni (average = 0.54 wt% ± 0.88 wt%) are detected. Variable As (average = 43.46 wt% ± 0.96 wt%) and S (average = 20.48 wt% ± 0.66 wt%) concentrations are consistent with other sulfarsenides. Au is below detection limits and therefore unable to be quantified.
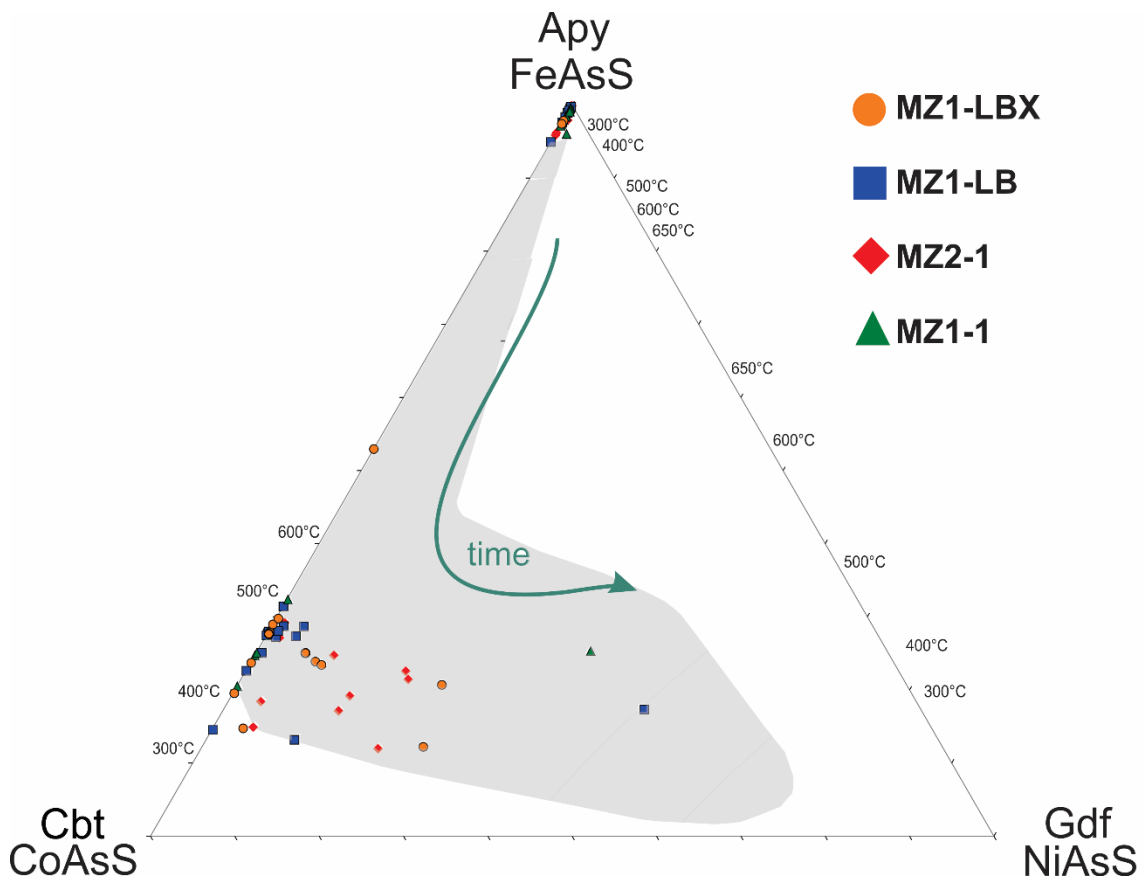
Figure 16: EPMA analyses of all mineralized veins plotted on a FeAsS-CoAsS-NiAsS ternary diagram showing the distribution of sulfarsenide phases in the assemblage over time (i.e. green time line). The grey field represents the range of analyses reported by Markl et al. (2016) of five element vein deposits in Germany.

Table 2: Representative EPMA analyses (wt%) of each sulfarsenide phase measured in all mineralized samples.

	MZ2-1			MZ1-LBX			MZ1-1		MZ1-Lb		
	Aspy	Fe-rich Cbt	Fe-Co-rich Grdf	Aspy	Fe-rich Cbt	Fe-Co-rich Grdf	Aspy	Fe-rich Cbt	Aspy	Fe-rich Cbt	Fe-Co-rich Grdf
Fe	33.22	5.40	7.638	25.76	0.87	19.652	33.71	8.89	34.93	10.33	4.805
Co	0.53	29.10	20.92	10.51	33.38	7.379	0.90	26.58	0.37	26.05	27.818
Ni	0.17	1.71	7.069	<0.03	<0.03	8.632	<0.03	0.03	<0.03	0.41	3.823
O	N/A	<0.03	<0.03	0.321	0.37	0.917	N/A	<0.03	0.893	0.16	0.114
As	42.35	43.48	44.155	43.86	43.37	41.962	40.96	44.33	39.67	43.40	44.169
Si	N/A	<0.01	<0.01	<0.02	<0.01	0.287	N/A	<0.01	0.011	0.02	0.032
Te	<0.02	0.02	0.068	<0.02	<0.02	0.063	<0.02	<0.02	<0.02	<0.02	0.032
Ag	<0.02	<0.06	<0.06	<0.02	<0.02	<0.02	<0.02	<0.06	<0.02	<0.02	<0.02
Au	<0.03	<0.03	<0.03	<0.03	<0.03	<0.03	<0.03	<0.03	<0.03	0.03	<0.03
S	21.53	20.51	19.478	20.27	21.44	20.427	23.08	19.84	23.48	20.78	19.586
Bi	0.30	<0.12	<0.05	<0.03	<0.05	<0.05	0.03	<0.12	<0.03	<0.06	<0.06
Sb	0.09	<0.03	<0.03	<0.03	<0.03	<0.03	0.03	<0.03	<0.03	<0.03	<0.03
Total	98.2	100.24	99.33	100.75	99.49	99.32	98.72	99.67	99.37	101.19	100.382

*Abbreviations are as followed: Aspy = Arsenopyrite, Fe-rich Cbt = Fe-rich Cobaltite, and Fe-Co-rich Grdf = Fe-Co-rich Gersdorffite

The chemistry of Co-Fe rich gersdorffite is quantified via 9 measurements (**Appendix Table 20**). The Co-Fe gersdorffite are the most enriched in Ni (average = 6.66 wt% ± 2.42 wt%) relative to adjacent the other sulfarsenide phases. The Fe concentrations (average = 12.15 wt% ± 7.82 wt%) are similar to Fe-rich cobaltite. High concentrations of Co are detected (average = 17.00 wt% ± 8.92 wt%) and are relatively variable. The As (average = 44.17 wt% ± 1.12 wt%) and S (average = 19.61 wt% ± 0.43 wt%) contents are invariable and similar to the levels in other sulfarsenides. The Au concentration was below detection limits and unable to be quantified.

S-isotope data

The bulk S-isotope values for the sulfarsenides between the three samples were determined via 15 measurements (**Table 3**). Values are similar, ranging from 3.9 to 6.6‰ $\delta^{34}S$. Minor variability is observed between the two main zones, whereby laminated sulfarsenides from MZ1 average 6.0 ± 0.38‰ $\delta^{34}S$ and sulfarsnenide mineralized clasts from MZ2 average 4.2 ± 0.27‰ $\delta^{34}S$.

Table 3: S-isotope analyses of mineralized veins MZ1-Lb, MZ1-LBX, and MZ2-1

Sample	$\delta^{34}S$
MZ1-Lb	6.0
MZ1-Lb	5.9
MZ1-Lb	6.1
MZ1-Lb	6.5
MZ1-Lb	6.6
MZ1-LBX	5.8
MZ1-LBX	5.6
MZ1-LBX	5.7
MZ1-LBX	5.9
MZ1-LBX	5.4
MZ2-1	3.9
MZ2-1	4.6
MZ2-1	4.1
MZ2-1	4.1
MZ2-1	4.4

Whole Rock Geochemistry

Whole-rock analyses for major, minor and trace elements were determined for mineralized and unmineralized samples.

Major elements for all unmineralized samples are listed in **Appendix Table 21.** Trace element measurements are presented in **Appendix Table 22**.

Elemental concentrations are measured for both mineralized samples (MZ1-Lb and MZ2-1) representing both main zones. Geochemical results are shown in **Appendix Table 23** and **Appendix Table 24.** Concentrations of metals of interest are as follow: Fe (MZ1-Lb = 23440 ppm; MZ2-1 = 38778.5 ppm), Co (MZ1-Lb = > 1500 ppm; MZ2-1 = > 1500 ppm), Ni (MZ1-Lb = 291 ppm; MZ2-1 = 1349 ppm), As (MZ1-Lb = > 7700 ppm; MZ2-1 = > 7700 ppm), Au (MZ1-Lb = 1.561 ppm; MZ2-1 = 18.091 ppm), and Bi (MZ1-Lb = 32.29 ppm; MZ2-1 = 57.91 ppm).

Discussion

Detailed field and micro-analytical work were completed in order to evaluate the: i) relative timing of the NFDO with respect to the spatially associated intrusions, ii) the vein paragenesis and implications of zoning, iii) the mafic and metasedimentary rocks as potential sources of the metals, iv) the source of sulfur, v) potential reductants for mineralization, nature of the fluids associated with the mineralization, and iv) formation conditions required for the mineralization. The above results will allow for the construction of a genetic model for the NFDO.

Relative Timing and Paragenesis of the NFDO and Associated Rocks

It is important to understand the timing of events and paragenesis of the mineralization and nearby lithologies in order to evaluate the genetic relationships and sources of metals and fluids for the NFDO. The Silurian-aged Kentville Formation metasediments are intruded by the gabbro and diabase sills (**Figure 3, Figure 5**). This is evidenced by distinct contact metamorphic haloes around the margins of the intrusions and lack of foliation, strain, or deformation in the mafic rocks (**Figure 5**). Although the lack of these structural features could be due to higher competence and crystalline nature of the mafic rocks relative to the metasediments during metamorphism, the preserved contact aureole indicates the gabbros postdate metamorphism. Two types of mafic intrusions occur in the Meguma Terrane: Type I predate regional metamorphism and Type II are associated with the SMB after metamorphism (Barr et al., 2003). Textural relationships suggest mafic rocks of the NFDO are Type II. The gabbro and diabase sills are locally crosscut by the felsic dykes, presumably of the Cloud Lake Pluton, suggesting the mafic intrusions predate ~380 Ma (**Figure 5**). The mafic intrusions were inspected for zircons and baddeleyite using SEM and samples were sent for mineral separates in order to evaluate whether absolute ages could be obtained. However, the amount and size of zircon and baddeleyite in the samples were too low. The rocks do contain apatite, which is dateable using the U-Pb chronometer; however, the closure temperature of apatite is low (approximately 500°C; Cherniak et al., 1991) and would have likely been reset during emplacement of the Cloud Lake Pluton.

Two types of quartz veins occur in the NFDO: fault hosted mineralized veins crosscut the Kentville Formation metasediments and barren quartz veins that crosscut the

mineralized veins, metasediments and Cloud Lake Pluton (**Figure 3, Figure 5, and Figure 6**). Fluid inclusion work on the quartz veins by Kennedy (2019) suggest that the fluids that produced all the vein types are similar and that they are all genetically related. This suggests the mineralizing event occurred after the emplacement of the SMB. Unfortunately, minerals suitable for radiometric age-dating were not observed within the mineralized veins.

Both styles of mineralized veins have a similar paragenesis, consisting of: i) early chlorite, biotite, and rutile occurring as laminations, wall rock clasts, and interstitial material to sulfarsenides (**Figure 8**), ii) pyrite and galena occurring as rounded inclusions in sulfarsenides (**Figure 8**), iii) zoned sulfarsenides consisting of euhedral arsenopyrite cores, mantled by cobaltite, and gersdorffite rims (**Figure 8**), and iv) late quartz surrounding and interstitial to the sulfarsenides (**Figure 8**, **Figure 9**). The interstitial chlorite, biotite, and rutile are likely inherited from the wall rock metasediments, as these phases are present in mineralization styles and consistent with the mineralogy of sample KF-1. The metasediments outside the veins contain a higher biotite content than chlorite with ilmenite and lesser rutile (**Figure 11**). The wall rock material in the veins contains a high abundance of chlorite and rutile, with lesser amounts of biotite and no ilmenite (**Figure 8**). This suggests mineralizing fluids chloritized the biotite of the wall rock, forming secondary chlorite and rutile. Rounded sulfide inclusions (e.g. pyrite) in the quartz veins mineral assemblage are possibly inherited from the metasediments, and were partially dissolved prior to sulfarsenide mineralization. However, sulfides could be products of early hydrothermal activity that were partially dissolved by later hydrothermal fluids. In both types of mineralization, sulfarsenides consist of early, euhedral arsenopyrite, mantled by arsenopyrite, cobaltite and rimmed by gersdorffite (**Figure 13, Figure 14**). The presence

50

of defined grain boundaries of the Fe-rich arsenopyrite cores mantled by later arsenopyrite indicate two generations of arsenopyrite are present **(Figure 14)**. Arsenopyrite is a common porphyroblast present in the Meguma Terrane metasediments (e.g., Kontak and Smith, 1998). It is possible that the early euhedral arsenopyrite cores are inherited from the wall rock metasediments; however, this is inconclusive due to the lack of evidence. Later arsenopyrite, cobaltite, and gersdorffite are interpreted to be a products of hydrothermal fluids.

Both styles of mineralization exhibit unidirectional zoning from Fe → Co → Ni-rich sulfarsenide **(Figure 13, Figure 14)**. The unidirectional zoning present in the laminated veins is consistent with settling of dense sulfarsenides at the base of the vein during crystallization as the fluids changed composition. The zoning can be explained by either i) fractionation of Fe, Co and then Ni from the fluid, or ii) a change in the fluids pH. Markl et al. (2016) suggests the zoning of sulfarsenides in five element vein systems is a result of changing pH, whereby Ni to Fe zonation reflects an increase in pH. However, this interpretation is based on the Fe-Co-Ni-O-Cl stability system because there is no available experimental data for sulfarsenides. If the sulfarsenide system is similar, the zoning pattern observed at the NFDO suggest a decrease in pH **(Figure 17)**. Experimental data on the stability of these phases is required in order to fully evaluate the cause of the observed zoning.
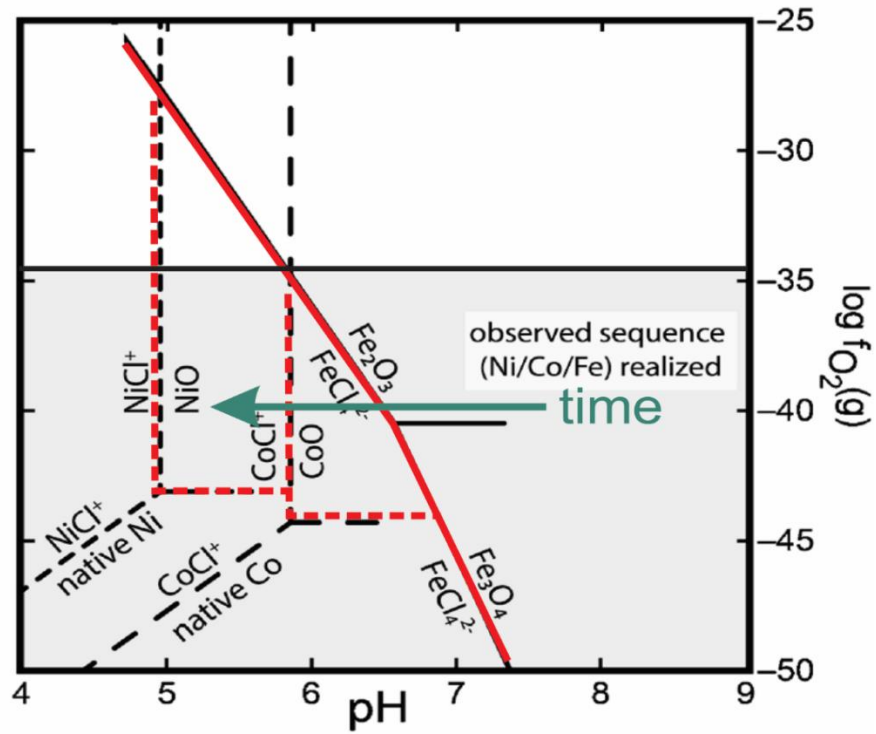
Figure 17: Stability diagram of Fe-Co-Ni-O-Cl system based on pH and fO_2 (modified by Markl et al., 2016). The green arrow indicates decreasing pH based on zoning of the sulfarsenides at the NFDO.

Potential Metal Sources

The two most likely sources for metals are the mafic intrusions and the Kentville Formation metasediments. Mafic intrusions are commonly thought to be sources of metals for five element type deposits (Kissin, 1992). The whole rock data for the mafic intrusions at the NFDO show high concentrations of cobalt and nickel (**Appendix Table 21**); however, these results are consistent with cobalt and nickel concentrations of surrounding mafic intrusions in the Meguma Terrane (**Figure 18**). Crosscutting relationships indicate mafic intrusions were emplaced prior to vein mineralization, confirming their potential of sources of metals as fluids may have leached Co and Ni from these rocks.

The Cape St. Marys cobalt-nickel occurrences are also associated, at least spatially, with mafic intrusions. The Cape St. Marys showings are hosted in the Cambrian-Ordovician aged Halifax Formation (O'Reilly, 1992) near the Mavillette gabbro plutons and proximal to related gabbroic sills (**Figure 1**). The mafic intrusions and mineralization in the Cape St. Marys area are located in the Cobequid Point Shear Zone (White et al., 2018). Both the Mavillette gabbro and the sills occur in the White Rock Formation, which is the lower unit of the Rockville Notch Group underlying the Kentville Formation (White et al., 2003). The White Rock Formation also hosts mafic volcanics. (White et al. 2002). Geochemical analyses for Co and Ni from the NFDO mafic rocks, as well as other mafic intrusions including those at Cape St. Marys are plotted in **Figure 18**, indicating similar Co and Ni contents.

Analyses of gabbroic rocks using SEM and micro-XRF imaging show high cobalt and nickel within the amphibole alteration of primary clinopyroxene (**Figure 15, Figure 12**). This indicates the cobalt and nickel enrichment of the mafic rocks is secondary.

Therefore, it is possible that mafic rocks are enriched by the mineralizing fluids rather than depleted. Alternatively, the mafic rocks were enriched by metasomatic fluids after emplacement. Dehydrations reactions in the contact aureole liberate fluids and metals which can react with the mafic intrusions that is producing cobalt and nickel-rich amphibole alteration. This process suggests the Kentville Formation metasediments as the primary source of metals.

The metasediments contains primary cobalt and nickel-rich sulfides, as indicated by SEM-EDS analysis (**Figure 11**). Bulk rock data show that the metasediments contain high concentrations of cobalt and nickel **(Appendix Table 22)**. The Meguma Terrane contains an abundance of metamorphosed organic-rich marine sediments. Organic-rich marine sediments typically contain elevated levels of metals, including those vented from hydrothermal fluids on the seafloor as well as those scavenged by Fe- and Mn-ferrihydroxides (Brumsack, 2006). Metasediments of the Meguma Terrane are suggested to be a variable source of metals for the NFDO; although, studies of the Cape St. Marys and other cobalt occurrences are needed to confirm this.
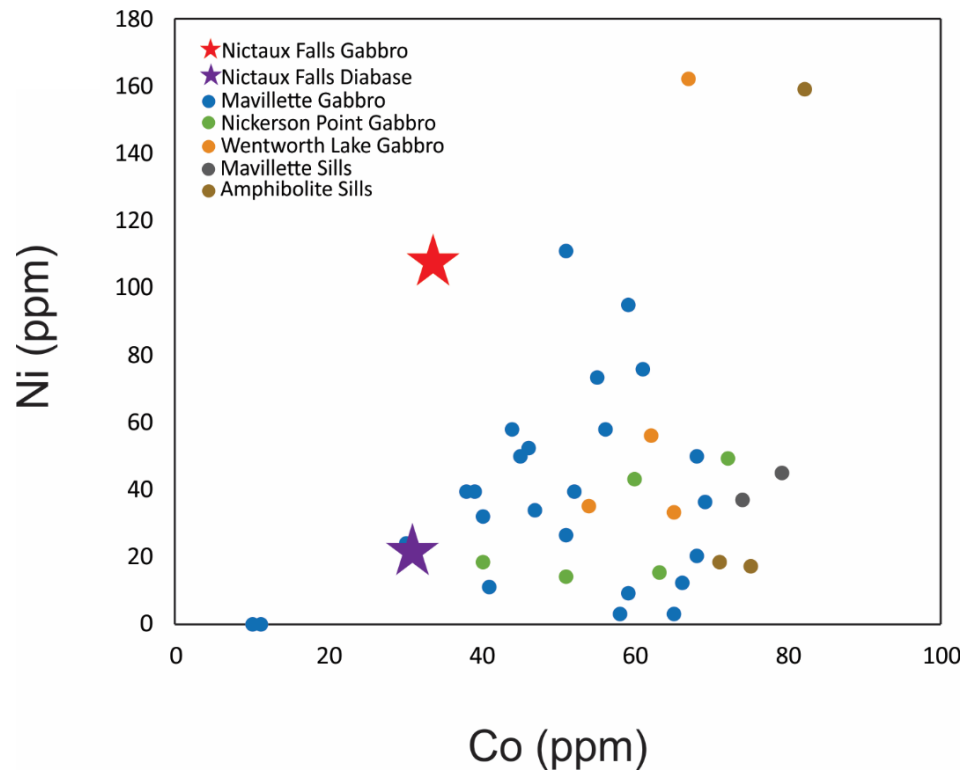
Figure 18: Representative diagram comparing Co-Ni concentrations of mafic intrusions in the Nictaux Falls and Cape St. Mary area

Potential Sulfur Source

Both Main Zone vein types are characterized by a narrow range of bulk δ^{34}S values. The relatively uniform δ^{34}S measurements, ranging from 3.9-6.6‰ δ^{34}S, tentatively suggests a well-homogenized source. However, in situ analysis is required in order to confirm one sulfur source.

Carboniferous-aged marine brines and the Kentville Formation metasediments are the most likely sources of sulfur and fluids for the NFDO. Fluid inclusion work by Kennedy (2019) suggests marine brines of the Carboniferous Maritimes Basin as the source of mineralizing fluid. The δ^{34}S of seawater varies over geological time. Mississippian-aged marine sulfate minerals indicate a seawater sulfate value of 17‰ δ^{34}S (**Figure 19**). There is no experimental data available for sulfarsenide systems; therefore, pyrite is used as a proxy. This is justified because of the structural similarities between pyrite, arsenopyrite and cobaltite, and similar δ^{34}S values are reported for coeval pyrite and arsenopyrite (Kontak and Smith, 1998). Based on the estimated temperatures (e.g. 250ºC and 400ºC; Kennedy, 2019), the fractionation between pyrite and seawater sulfate are estimated to be 26.2‰ at 250°C and 16.4‰ at 400°C (Figure 19). Therefore, if the source of sulfur is Mississippian seawater, the δ^{34}S values at 250°C and 400°C would be -9‰ and 0‰, which is lower than the bulk δ^{34}S if this study.

Kontak and Smith (1988) investigated δ^{34}S values of arsenopyrite present in Meguma Terrane saddle-reef gold deposits, and reported values of approximately 10.5 ‰. Even though the arsenopyrites of the Meguma Gold deposits are hydrothermal in origin, Kontak and Smith (1998) suggest the sulfur was sourced from the local metasediment

56

sulfides. The δ^{34}S values of the NFDO are slightly lower than the arsenopyrites from the Meguma Gold deposits.

In order to evaluate the source of sulfur, bulk δ^{34}S values of the NFDO have been plotted with δ^{34}S values of arsenopyrite in the Meguma Terrane (e.g. metasedimentary origin; Kontak and Smith, 1998) and theoretical pyrite from Mississippian seawater (e.g. marine brine origin; **Figure 19)** at 250 to 400°C (temperature range from Kennedy 2019). The δ^{34}S range for the NFDO lies between both the metasediment and marine brine origins, suggesting mixing of these two sources. However, the bulk δ^{34}S for the NFDO does not resolve the δ^{34}S for individual sulfarsenide phases, which is required in order to evaluate fluid mixing. Therefore, details regarding possible fluid mixing events are unclear and the source of sulfur are inconclusive pending in situ SIMS δ^{34}S results.
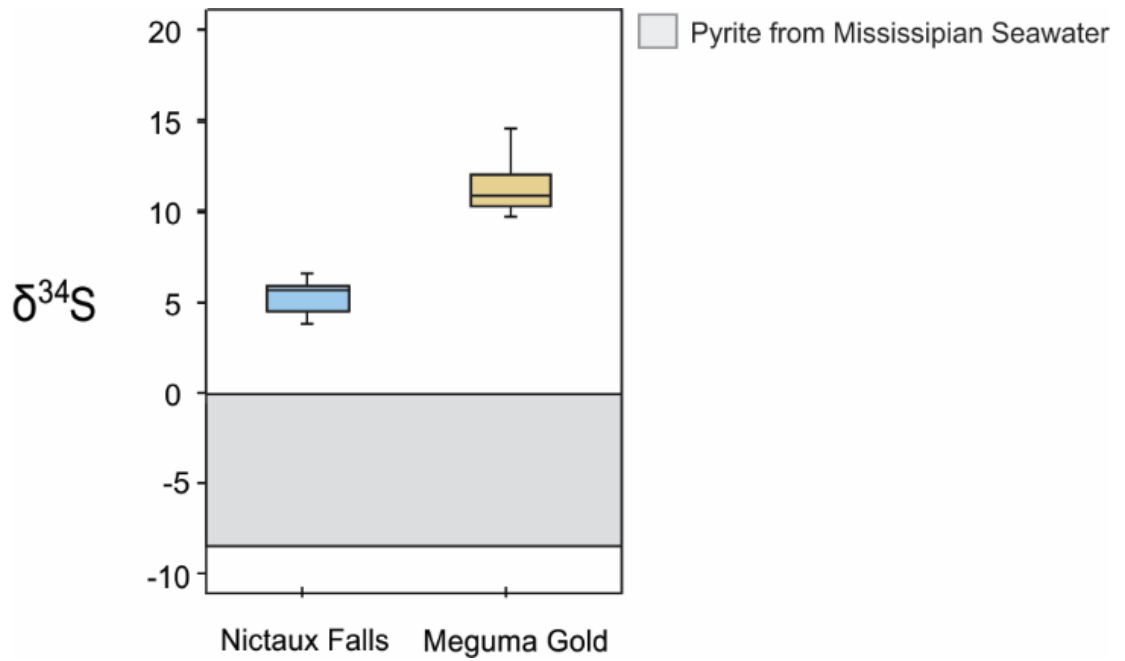
Figure 19: Sulfur isotope range of the sulfarsenides from the NFDO and arsenopyrite from the Meguma Gold deposits (Kontak and Smith, 1998). Grey field represents the S-isotope range of pyrite from Mississippian seawater at 250 to 400°C.

Potential Reductants

Sulfarsenides are stable in a reduced environment, as sulfur and arsenic are present in their reduced state (S^{2-} and As^{1-} respectively; Hem and Makovicky, 2001). Arsenic is present in hydrothermal fluids associated with cobalt-nickel vein deposits as arsenate complexes (H_3AsO_3 or AsO_3^{3-}; Markl et al., 2016); therefore, the mechanism for ore formation requires a reductant. Two of the most likely reductants in this system are Fe^{2+} and CH_4. Ferrous iron occurs in Fe-bearing silicate minerals, such as biotite and chlorite, as well Fe-bearing sulfides and oxides (e.g. pyrite and ilmenite; **Figure 11**) in the metasediments. The metasediments as a reductant is supported by the close spatial relationship between the metasediments and the mineralization. Hydrothermal fluids responsible for vein formation also chloritized biotite of the wall rock. This reaction can liberate Fe^{2+}, which can serve as a reductant. However, the chlorite should contain lower Fe^{2+} than biotite. This is not observed, suggesting that Fe^{2+} was not liberated or served as the reductant **(Appendix Table 1)**. Alternatively, Fe-rich sulfides (e.g. pyrite) and oxides (i.e. ilmenite and magnetite) in the wall rock are also a potential reductant. Petrographic study indicates early rounded pyrite inclusions in the sulfarsenide veins (**Figure 8**). The rounded nature of the sulfides suggests the minerals were partially dissolved prior to sulfarsenide mineralization. In addition, the alteration of metamorphic ilmenite present in the Meguma metasediments to rutile releases Fe^{2+}. Thus, these processes could have supplied the Fe^{2+} necessary to form sulfarsenides. If Fe^{2+} is the reductant, its oxidation to Fe^{3+} could produce hematite or magnetite, which is not observed in the NFDO mineral assemblage. The lack of these Fe-oxides can be explained by high Cl^- and low pH, creating unfavorable conditions (Ding and Seyfried, 1992). Fluid inclusion work by Kennedy (2019) indicates a high Cl^- content (from 29-35 wt% NaCl equivalent) in the mineralizing fluids.

Additionally, the zoning of the sulfarsenides suggests low pH late in the paragenesis **(Figure 17)**.

According to Markl et al. (2016), CH_4 is a possible reductant in five element vein type deposits as it is detected in some carbonate hosted fluid inclusions. Trace amounts of methane occur in the fluid inclusions of the NFDO (Kennedy, 2019). As the origin of CH_4 can vary for five element type deposits (Markl et al., 2016), the methane from the NFDO is possibly sourced from the abundant organic matter in the Meguma Terrane. Reduced carbon from carbonaceous material of the Meguma Terrane metasediments is proposed as the reductant in the formation of Meguma Gold deposits (Bierlein et al., 2004). Therefore, CH_4 is another possible reducing agent in this system.

Genetic Model for the NFDO

Based on integrated results by this study and Kennedy (2019), the NFDO formed from marine brines after the emplacement of the SMB. The most likely source of seawater would be the Mississippian-age evaporite sequences of the Maritimes Basin. Marine brines derived from seawater from the overlying Windsor Group evaporites are suggested because fluid inclusion analyses show high salinity, and high Ca^{2+} and Na^+ with low K^+ (Kennedy, 2019). The fluid inclusion work also suggests the presence of two fluids of marine origin: Na-rich marine brine and a Ca-rich evolved brine, which was product of the Na-rich fluid equilibrating with the plagioclase-bearing basement rocks. Late Paleozoic regional scale shear structures provide conduits for marine brines to migrate to the Meguma Terrane basement rocks (Giles, 1985). Textural evidence paired with S-isotope work suggest some key components (e.g. Fe, S, metals) were extracted from the metasediments, and that the metasediments may have provided a reductant for mineralization (e.g. reduced Fe or

methane). Marine brines may have also supplied some sulfur; however, in situ $\delta^{34}S$ work is required to evaluate fluid mixing.

Five Element Vein Deposits

There are key similarities as well as differences between the NFDO and five element vein deposits based on the respective mineral assemblages, compositional zoning, paragenetic sequences, and textures. Petrographic study of the NFDO indicates a less complex mineral assemblage compared to typical five elements vein deposits. Similarities include discrete stages of native metals (e.g. Au-Ag alloy), a sulfarsenides, sulfides (e.g. pyrite), late gangue (e.g. quartz), and compositional zoning. However, the NFDO assemblages lack specific components of five elements vein deposits (Markl et al., 2019; Kissin, 1992). Although a distinct native metal stage occurs in the NFDO, a Au-Ag alloy is present rather than native silver and bismuth, which characterizes five elements deposits. This compositional difference could be due to the abundant gold hosted in the Meguma Terrane. Although native bismuth is not observed in the NFDO assemblage, bulk rock analyses show 32.3 – 58.5 ppm Bi, suggesting bismuth is substituting for arsenic in sulfarsenides. Microprobe analysis confirms up to 3000 ppm Bi (**Appendix Table 18**). Di- and tri- arsenide minerals (As^{2-} and As^{3-}) are absent in the NFDO; however, it is possible the fS_2 or fO_2 were too high to form arsenide phases. A distinct sulfide stage in the NFDO occurs as rounded pyrite inclusions in the sulfarsenides (**Figure 8**); however, its origin is unclear. The sulfides could be inherited from the wall rock, or a product of hydrothermal activity and partially dissolved prior to sulfarsenide mineralization. Although the sulfarsenides show compositional zoning in the NFDO, an opposite zoning pattern is exhibited (Fe→ Co→ Ni; **Figure 13**), suggesting a decrease in pH rather than an increase

(Markl et al., 2016). Another difference noted is the presence of quartz rather than carbonates in the NFDO; however, the low pH suggested by the zoning pattern could also explain the precipitation of quartz over carbonates **(Figure 17)**.

Although native metals (i.e. Au and Ag) occur in the NFDO, they are paragenetically late in the mineral assemblage, as they are hosted interstitial to the Fe-Co-rich gersdorffite. However, in typical five elements vein deposits, native metals (e.g. silver and bismuth) are one of the first phases to form (Markl et al., 2016).

Textural similarities between the NFDO and five elements vein sulfarsenides are observed as sulfarsenides occur as blocky, euhedral grains. For example, the NFDO textures are similar to that of the Great Slave Lake five elements veins in the Northwest Territories (Burke, 2019). In five elements deposits, native metals exhibit skeletal/dendritic textures (Markl et al., 2016). This is not observed at the NFDO. Contrastingly, the Au-Ag alloy exhibits fracture infilling texture, as it occurs interstitial to the Fe-Co-rich gersdorffite **(Figure 10)**.

Based on the similarities and differences noted between the NFDO and a typical five element vein deposit, the NFDO may be a unique example of five element vein occurrence. More in depth study of cobalt occurrences in the Meguma Terrane are needed in order to understand the metallogeny of this occurrence.

Conclusions

The NFDO is a unique vein system that postdates the SMB. Petrographic study and bulk rock data suggest the Kentville Formation metasediments as the potential source of metals for the NFDO. Bulk $\delta^{34}S$ values tentatively suggest the sulfur is sourced from both

metasediments and marine brines derived from the Carboniferous Maritimes Basin. This can be confirmed by in situ $\delta^{34}S$ work. The NFDO contains similar components to that of five element type deposits; however, the lack of certain components can be explained by different formation conditions (e.g. fO$_{2,}$ fS$_2$, pH). The NFDO may be a unique example of a five elements vein occurrence in Nova Scotia, because of the local geology. Cobalt occurrences in Nova Scotia require further evaluation in order to understand the cobalt metallogeny of Nova Scotia.

Acknowledgements

To many of the SMU faculty, staff, and my fellow lab mates, you're all to blame for what I've become. Thank you to my supervisor Dr. Erin Adlakha (i.e. the lady who emails me at 2AM), to whom I owe my ability to distinguish between apples and oranges. My smoothies have improved greatly since meeting you. To Dr. Jacob Hanley, you've taught me that it's socially acceptable to wear the same shirt three days in a row; however, that blue shirt is getting old and you should take your daughter Chinchilla shopping with you. You also taught me how to envision every room as a magma chamber, going to church is really weird now. Thank you to Mitch Kerr and Kevin Neyedley for ensuring Erin was sufficiently full of wings and wine that she could put up with my "smarmy" personality. Also, smarmy is not a word. To my work supervisor Dr. Geoff Baldwin, I have become much more cynical over the past year and I believe you're almost 100% of the blame. Thank you to my fellow lab mates, not for your support, but for your excessive crying and whining that now allows me to work from my own home.

This thesis can be referred to as my prolonged period of self-deprecation and suffering, and I blame all of you for this. My tendency to not smile has become a popular joke throughout this year and I just want to clarify that it's not that my face rests like this, but because I just don't like any of you.

References

Andrews, A. J., Owsiacki, L., Kerrich, R., & Strong, D. F. (1986). The silver deposits at Cobalt and Gowganda, Ontario. I: Geology, petrography, and whole-rock geochemistry. *Canadian Journal of Earth Sciences*, *23*(10), 1480-1506.

Barr, S. M., Doyle, E. M., & Trapasso, L. S. (1983). Geochemistry and tectonic implications of mafic sills in Lower Paleozoic formations of southwestern Nova Scotia.

Barr, S. M., Davis, D. W., Kamo, S., & White, C. E. (2003). Significance of U–Pb detrital zircon ages in quartzite from peri-Gondwanan terranes, New Brunswick and Nova Scotia, Canada. *Precambrian Research*, *126*(1-2), 123-145.

Bierlein, F. P., Christie, A. B., & Smith, P. K. (2004). A comparison of orogenic gold mineralisation in central Victoria (AUS), western South Island (NZ) and Nova Scotia (CAN): implications for variations in the endowment of Palaeozoic metamorphic terrains. *Ore Geology Reviews*, *25*(1-2), 125-168.

Brumsack, H. J. (2006). The trace metal content of recent organic carbon-rich sediments: implications for Cretaceous black shale formation. *Palaeogeography, Palaeoclimatology, Palaeoecology*, *232*(2-4), 344-361

Burisch, M., Gerdes, A., Walter, B. F., Neumann, U., Fettel, M., & Markl, G. (2017). Methane and the origin of five-element veins: mineralogy, age, fluid inclusion chemistry and ore forming processes in the Odenwald, SW Germany. *Ore Geology Reviews*, *81*, 42-61.

Cormier, C. F. M., Barr, S. M., & Dunning, G. R. (1995). Geological setting and petrochemistry of early Middle Devonian volcanic and gabbroic rocks in the Guysborough area, Nova Scotia.

Ding, K., & Seyfried Jr, W. E. (1992). Determination of Fe-Cl complexing in the low pressure supercritical region (NaCl fluid): Iron solubility constraints on pH of subseafloor hydrothermal fluids. Geochimica et Cosmochimica Acta, 56(10), 3681-3692.

D.J. Cherniak, W.A. Lanford, F.J. Ryerson Lead diffusion in apatite and zircon using ion implantation and Rutherford backscattering techniques Geochim. Cosmochim. Acta, 55 (1991), pp. 1663-1674Markl, G., Burisch, M., & Neumann, U. (2016). Natural fracking and the genesis of five-element veins. *Mineralium Deposita*, *51*(6), 703-712.

Gibling, M. R., Culshaw, N., Rygel, M. C., & Pascucci, V. (2008). The Maritimes Basin of Atlantic Canada: basin creation and destruction in the collisional zone of Pangea. *Sedimentary basins of the world*, *5*, 211-244.

Giles, P.S. 1985. A major Post-Visean sinistral shear zone - new perspectives on Devonian and Carboniferous rocks of southern Nova Scotia. In Guide to the Granites and Mineral Deposits of Southwestern Nova Scotia. Edited by A.K. Chaterjee and D.B. Clarke. Nova Scotia Department of Mines and Energy, Paper 85-3, pp. 233-248.

Hem, S. R., Makovicky, E., & Gervilla, F. (2001). Compositional trends in Fe, Co and Ni sulfarsenides and their crystal-chemical implications: Results from the Arroyo De La Cueva deposits, Ronda peridotite, Southern Spain. *The Canadian Mineralogist*, *39*(3), 831-853.

Kennedy, N. (2019*). Fluid inclusion systematics of the polymetallic (Co-Ni-As-Au) veins of the Nictaux Falls Dam Occurrence, Annapolis Valley, Nova Scotia* (Unpublished BSc Honours Thesis). Saint Mary's University, Halifax, Nova Scotia.

Kissin, S. A. (1992). Five-element (Ni-Co-As-Ag-Bi) veins. *Geoscience Canada*, *19*(3).

Kontak, D. J., & Smith, P. K. (1989). Sulphur isotopic composition of sulphides from the Beaver Dam and other Meguma-Group-hosted gold deposits, Nova Scotia: implications for genetic models. *Canadian Journal of Earth Sciences*, *26*(8), 1617-1629.

MacDonald, M. A., & Clarke, D. B. (2017). Occurrence, origin, and significance of melagranites in the South Mountain Batholith, Nova Scotia. *Canadian Journal of Earth Sciences*, *54*(7), 693-713.

Markl, G., Burisch, M., & Neumann, U. (2016). Natural fracking and the genesis of five-element veins. *Mineralium Deposita*, *51*(6), 703-712

McKenzie, C. B., & Clarke, D. B. (1975). Petrology of the South Mountain Batholith, Nova Scotia. *Canadian Journal of Earth Sciences*, *12*(7), 1209-1218.

Ohta, E. (1991). Polymetallic mineralization at the Toyoha mine, Hokkaido, Japan. *Mining Geology*, *41*(229), 279-295.

O'Reilly, G. A. 1995: A little known Ni-Co-Bi-Sb-Pb-Ag-Au association in the Annapolis Valley; in Nova Scotia Minerals Update; Nova Scotia Department of Natural Resources, Mineral Resources Branch Newsletter, v. 6, Fall 1995

O'Reilly, G. A. 1992: Stop 1-8 Nictaux Falls Dam Prospect and the Co-Ni-As-Au±U association; Geological Association of Canada, Annual General Meeting – Wolfville 1992;

Field Trip Guidebook- Granite Associated Mineral Deposits of Southwest Nova Scotia, leaders G. A. O'Reilly, D. J. Kontak and M. A. MacDonald, p. 29-33

Seal, R. R. (2006). Sulfur isotope geochemistry of sulfide minerals. *Reviews in mineralogy and geochemistry*, *61*(1), 633-677.

Slack, J. F., Causey, J. D., Eppinger, R. G., Gray, J. E., Johnson, C. A., Lund, K. I., & Schulz, K. J. (2010). *Co-Cu-Au deposits in metasedimentary rocks-A preliminary report*.

Slack, J. F. (2012). Strata-bound Fe-Co-Cu-Au-Bi-Y-REE deposits of the Idaho cobalt belt: Multistage hydrothermal mineralization in a magmatic-related iron oxide copper-gold system. *Economic Geology*, *107*(6), 1089-1113.

Shellnutt, J. G., Owen, J. V., Yeh, M. W., Dostal, J., & Nguyen, D. T. (2019). Long-lived association between Avalonia and the Meguma terrane deduced from zircon geochronology of metasedimentary granulites. *Scientific reports*, *9*(1), 4065.

White, C. E., & Barr, S. M. (2012). Meguma Terrane revisited: stratigraphy, metamorphism, paleontology, and provenance. *Geoscience Canada*, *39*(1).

White, C., & Barr, S. (2017). Stratigraphy and depositional setting of the Silurian–Devonian Rockville Notch Group, Meguma terrane, Nova Scotia, Canada. *Atlantic Geology*, *53*, 337-365.

White, C. E., Barr, S. M., & Linnemann, U. (2018). U–Pb (zircon) ages and provenance of the White Rock Formation of the Rockville Notch Group, Meguma terrane, Nova Scotia, Canada: evidence for the "Sardian gap" and West African origin. *Canadian Journal of Earth Sciences*, *55*(6), 589-603.

Appendix

Appendix Petrography

Sample N1-11-G, which represents the least altered monzogranite, is coarse grained and characterized by primary plagioclase (30 modal%), quartz (24%), Fe-rich biotite (22%), K-feldspar (19%) with lesser amounts of muscovite (5%). Plagioclase is euhedral (4 to 6 mm) and present as megacrysts throughout the rock **(Appendix Petrography 1A),** surrounded by a groundmass of anhedral quartz (500 µm), K-feldspar (50 to 80 µm) and lathlike biotite and muscovite (80 to 300 µm; **Appendix Petrography 1B,C&D).** Primary biotite hosts secondary ilmenite within cleavage planes, as well as subhedral fluorapatite and zircon **(Appendix Petrography 1E&F)**. Related samples (i.e. GR-1, FD6, GDY1, GDY2, and GRSN) demonstrate a similar major mineral assemblage relative to N1-11-G, with the exception of secondary and trace minerals. Analysis using SEM identified pyrite, chalcopyrite, galena, arsenopyrite, chlorite, and rutile **(Appendix Petrography 1F)**. In addition, apatite contains detectable quantities of cobalt and nickel via EDS analysis.
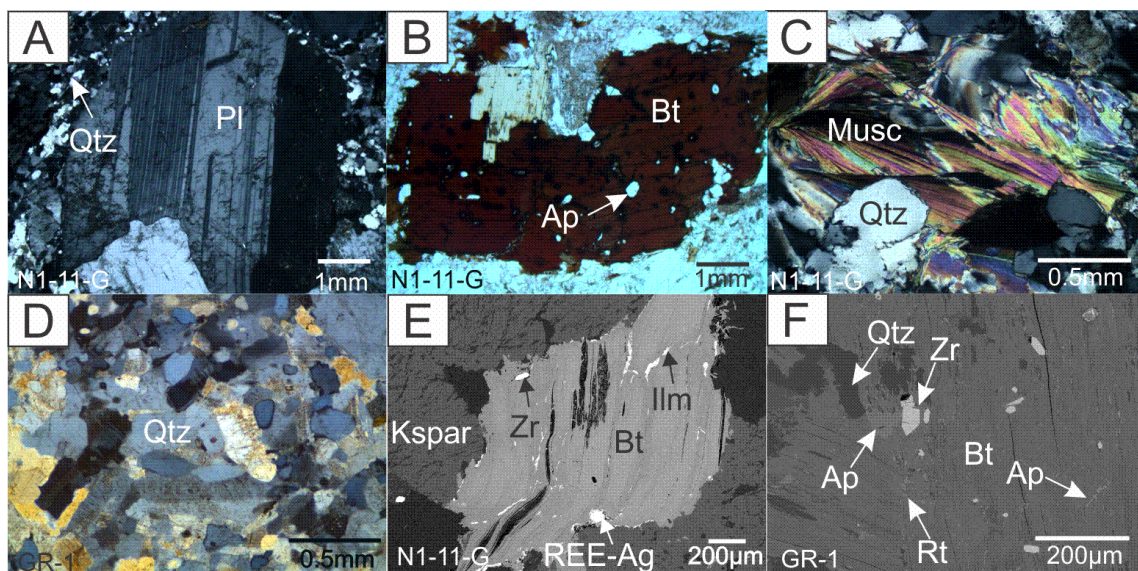
Appendix Petrography 1: Representative images of the main mineralogy of granitic samples. A) A photomicrograph of primary plagioclase surrounded by anhedral quartz in sample N1-11-G. B) A photomicrograph of lath-like biotite hosting inclusions of subhedral zircon in sample N1-11-G. B) A photomicrograph of lath-like biotite hosting inclusions of subhedral zircon in sample N1-11-G. C) A photomicrograph of lath-like muscovite surrounded by anhedral quartz in samples N1-11-G. D) A photomicrograph of variable sized anhedral quartz in samples GR-1, likely a resolute of quartz flooding. E) A BSE image of primary biotite hosting anhedral ilmenite, subhedral zircon, and a cluster of REE-Ag minerals surrounded by K-feldspar in sample N1-11-G. F) A BSE image of primary biotite hosting traces of blebby rutile and euhedral fluorapatite and zircon, surrounded by anhedral quartz in sample GR-1.

Quartz veins in samples QVY, QVZ, and GRBX are barren with respect to sulfarsenide mineralization and consist of mainly anhedral quartz. The granite from GRBX near the veins is characterized by primary quartz and Fe-rich biotite. Quartz is anhedral (40 to 100 µm) occurring brecciated and crosscut by quartz veins across the sample **(Appendix Petrography Fig. 2A).** Biotite (100 to 350 µm) is dispersed throughout the sample and is altered to chlorite in select areas **(Appendix Petrography 2B).** Brecciated quartz in GRBX is comparable to QVY and QVZ; however, primary biotite in GRBX has altered to

intermediate chlorite, hosting inclusions of ilmenite as individual euhedral grains or disseminated within the grain **(Appendix Petrography 2C&D).**
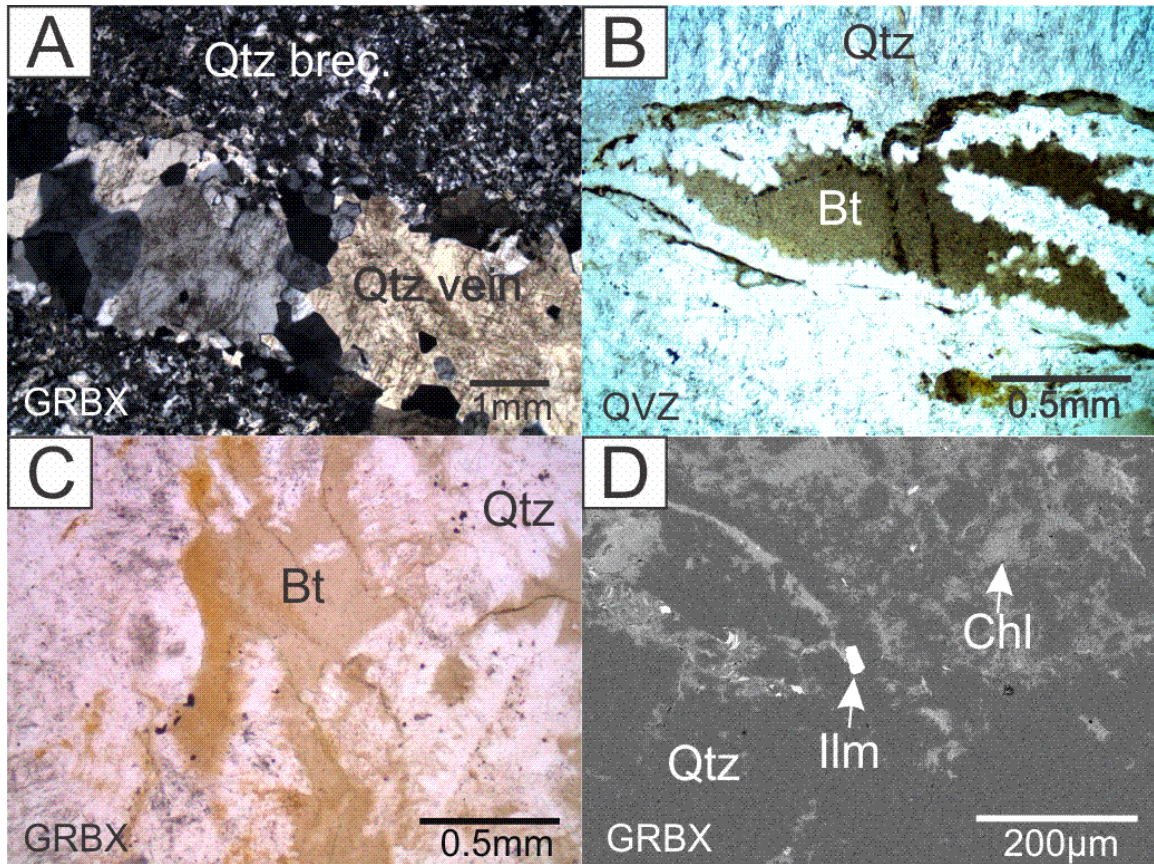
Appendix Petrography 2: Representative images of the main mineralogy in sample GRBX. A) A photomicrograph of quartz occurring as veins or brecciated in local areas. B) A photomicrograph of low-grade biotite surrounded by primary brecciated quartz. C) A BSE image of small, anhedral ilmenite occurring in secondary chlorite alteration surrounded by primary quartz.

Appendix Table 1: SEM analyses (wt%) of silicate minerals in the Kentville Formation metasediment sample (KF-1).

	Biotite			**Chlorite**		**K-feldspar**
O	49.2	48.89	50.81	53.88	53.89	51.29
Mg	5.71	5.58	7.05	8.7	6.2	
Al	8.72	8.63	10	10.55	9.87	8.55
Si	15.82	15.98	14.41	11.06	12.58	28.04
K	6.87	6.95	3.51		0.73	11.85
Ti	1.21	1.59	0.47			
Fe	12.46	12.38	13.75	15.8	16.72	0.26

Appendix Table 2: SEM analyses (wt%) of sulfides and oxides in the Kentville Formation sample (KF-1).

	Pyrite													Ilmenite			
Si	0.15	0.34	0.2	0.13			0.17	0.44	0.21	0.18	0.18	0.15	0.19	0.19	0.19	0.19	0.25
S	56.43	56.45	56.4	56.9	56.75	56.67	56.77	56.8	56.88	56.61	56.57	56.71	56.66				
Fe	43.41	42.77	42.61	42.97	43.25	43.33	43.06	42.76	42.91	43.21	43.24	43.14	43.15	29.76	29.44	29.65	29.75
Ti														27.85	27.67	27.89	27.76
Mn														1.74	1.91	1.75	1.96
O														40.47	40.79	40.52	40.27
Ni		0.44	0.79														

	Amphibole																																				
O	57.14	51.95	53.47	53.55	54.19	53.57	53.88	52.92	53.11	53.44	56.54	53.53	53.63	52.79	52.93	52.71	54.28	53.18	52.57	54.36	54.06	53.83	53.85	52.75	53.77	52.87	52.49	53.05	52.5	53.1	55.19	54.64	53.05	53.79	52.98	54.07	52.71
Na						0.52		1.6	1.63	1.25				1.84	1.22	1.41		1.18	1.88	2.77		0.97		0.83		1.53	0.97	1.04	1.73	1			1.46		1.3		1.7
Mg	1.22	4.28	5.05	5.77	5.68	3.76	4.98	6.47	6.32	6.73	6.69	6.17	7.32	6.1	6.74	6.65	6.57	6.39	6.36	3.68	7.65	7.48	6.46	8.2	6.77	6.09	8.26	7.44	6.05	7.48	7.86	7.68	6.55	7.59	6.55	6.34	6.16
Al	7.33	0.59	3.64	3.29	2.17	5.69	4.09	5.88	5.84	5.82	9.47	5.73	8.75	6.36	5.13	5.4	5.62	6.24	6.49	9.13	7.77	4.44	5.93	3.03	8.33	5.93	4.13	4.96	6.36	4.82	8.72	8.88	5.62	8.22	5.83	5.76	5.83
Si	16.77	21.59	20.89	21.2	21.28	19.39	20.3	18.92	18.65	18.72	13.9	19.81	15.26	18.36	19.86	19.51	19.3	18.48	18.31	21.23	15.87	19.93	19.16	21.25	15.24	18.12	20.86	19.85	18.43	19.41	14.13	14.55	18.98	14	18.81	19.33	18.66
K				0.14	0.33		0.25		0.19	0.28	1.16		5.57	0.2		0.25	0.18	0.21	0.24			1.74		0.26			5.22	0.25	0.25	0.84	3.15	3.39	0.18	3.66	0.32	0.28	0.24
Ca	6.5	12	6.57	6.49	6.31	6.18	6.48	5.55	5.53	5.35	3.48	5.8	0.26	5.58	6.17	5.29	5.86	5.92	5.72	5.81	1.86	4.82	5.83	4.17	0.99	5.74	6.41	6.29	5.74	3.85	0.51	0.64	5.57	0.21	5.63	5.77	5.71
Ti				0.17		0.17		0.2	0.38	0.72			0.43	0.21	0.21		0.28	0.27	0.18			0.23		0.59	0.3	1.63	1.03	0.44	0.71	0.18	0.2	0.37	0.29	0.17	0.3		0.2
Mn		0.27					0.24																								0.18						0.26
Fe	7.36	9.33	10.39	9.74	10.06	10.49	9.62	8.66	8.53	8.04	8.03	8.86	8.77	8.57	7.74	8.79	7.95	8.15	8.25	3.02	10.83	8.54	8.08	9.45	8.04	8.33	6.45	6.65	8.77	9.13	10.07	9.93	8.42	9.7	8.57	8.58	8.54

	Pyroxene										Biotite					Plagioclase								Allanite					Zircon				
O	51.95	52.25	52.25	52.26	54.93	53.55	53.47	52.61	51.87	54.88	52.49	51.58	51.83	52.07	52.36	55.35	54.72	55.12	54.79	55.16	54.69	53.99	54.53	57.26	57.14	57.49	56.95	51.08	42.59	41.41	42.16	42.05	40.56
Na																4.87	5.14	5.4	5.04	6.91	4.46	2.28	2.45	0.73	1.22	0.55	1.36	8.58					
Mg	4.28	5.66	4.84	4.95	4.07	5.77	5.05	5.73	4.81	0.42	7.03	7.59	7.24	7.71	8.26																		
Al	0.59		0.63		0.94	3.29	3.64		0.6	11.93	7.99	7.94	7.82	8.44	8.51	12.26	12.27	12.06	12.27	10.37	12.87	14.92	14.67	6.58	7.33	6.71	6.98	12.46					
Si	21.59	22.11	21.65	21.89	16.69	21.2	20.89	22.2	21.52	17.23	15.63	16.16	15.94	15.95	15.79	23.21	23.81	23.61	23.7	25.65	22.99	21.23	20.98	16.65	16.77	16.37	16.97	3.91	13.31	13.41	13.57	13.56	13.87
K											6.16	6.36	6.42	6.01	5.7																		
Ca	12	12.79	11.7	12.05	11.14	6.49	6.57	11.97	12.58	11.12						4.32	4.07	3.81	4.2	1.9	4.98	7.57	7.37	5.96	6.5	6.11	6.22	12.19					
Ti											1.04	1.14	1.33	0.41	0.16									0.22									
Mn	0.27		0.28	0.32				0.24	0.31																								
Fe	9.33	7.18	8.65	8.52	8.57	9.74	10.39	7.25	8.32	4.41	9.66	9.23	9.41	9.41	9.22									8.02	7.36	7.88	7.08	4.14					
Ce																								4.79	3.68	4.88	2.94	4.01					
Nd																											1.28	1.16					
La																												2.47					
Zr																													44.1	43.71	44.27	44.39	45.57
Hf																														1.47			

Appendix Table 4: SEM analyses (wt%) of sulfides and oxides from the gabbro at the NFDO (GB-1).

	Apatite																																	
O	50.39	50.26	50.35	50.37	51.24	49.62	50.3	50.36	50.54	50.44	50.36	49.88	49.78	50.17	49.54	50.13	50.41	49.99	50.45	49.71	49.54	49.88	50.51	50.28	49.84	49.95	49.73	49.31	48.13	50.13	49.23	49.61	49.55	50.09
Si	0.64	1.41	0.89	0.71	1.14	1.18	0.8	0.87	0.9	0.74		0.51	0.5	0.54	0.54	0.55	0.64	0.63	0.51	0.53	0.56	0.63				0.53	0.58		0.64			0.65		
P	17.78	17.46	17.77	17.89	17.07	18.32	17.6	17.68	17.6	17.88	17.93	18.14	18.08	17.64	17.71	17.94	17.69	17.89	17.82	17.92	17.86	17.68	17.83	18.08	17.84	18.05	18.11	18.37	19.02	18.13	18.32	17.81	18.33	17.93
Ca	31.19	30.05	30.5	31.04	30.06	30.88	30.9	30.7	30.5	30.56	30.67	31.26	31.26	30.5	30.65	30.79	31.01	30.9	30.6	31.09	30.75	30.18	30.75	31.23	31.31	31.14	31.57	31.51	32.21	31.74	31.9	31.12	31.85	31.13
Fe		0.82	0.48		0.5		0.4	0.39	0.46	0.37	1.03												0.26											
Cl												0.21	0.37	0.71	1.24	0.2		0.31	0.41	0.75	1.28	1.36	0.92	0.41	1	0.32		0.81			0.55	0.81	0.27	0.85
S																																		
Co																																		
Ni																																		
As																																		
Zr																																		
Ti																																		
Mn																																		

Element	Cobaltite					Pyrite								Baddeleyite		Ilmenite										
O														33.83	34.03	47.03	48.03	48	47.61	47.88	47	46.92	47.51	47.13	47.03	47.24
Si																										
P																										
Ca																										
Fe	4.55	4.54	4.52	4.31	4.53	52.11	53.31	53.25	53.18	53.53	53.59	53.54	53.71	0.54	0.55	26.05	24.89	24.96	25.01	24.96	26.2	26.02	25.98	26.23	26.04	25.96
Cl																										
S	22.38	22.29	21.94	22.14	22.28	47.89	46.69	46.75	46.12	46.47	46.41	46.46	46.29													
Co	18.19	18.16	18.05	19.09	18.09																					
Ni	5.05	4.87	5.88	4.66	5.58																					
As	49.84	50.13	49.61	49.79	49.51																					
Zr														65.63	64.92											
Ti																25.73	25.23	24.9	25.21	25.3	25.43	25.88	25.18	25.34	25.72	25.62
Mn																1.19	1.84	1.77	1.81	1.66	1.37	1.19	1.32	1.3	1.21	1.18

Appendix Table 5: SEM analyses (wt%) of the sulfides and oxides from the DB-1 sample in the NFDO.

	Pyrite										Sphalerite				Ilmenite			
O															47.6	47.16	47.29	47.48
S	46.19	46.77	46.13	46.07	46.25	46.16	45.88	45.8	46.1	45.97	40.56	40.79	41.31	41.16				
Fe	53.81	53.23	53.87	53.42	53.75	53.84	54.12	54.2	53.9	54.03								
Ni				0.5														
Ca																0.53	0.34	0.58
Ti															25.31	24.98	25.09	24.36
Mn															1.17	1.38	1.37	1.31
Fe											8.32	8.34	8.3	12.96	25.91	25.51	25.69	25.53
Si																0.45	0.23	0.74
Zn											51.12	50.87	50.39	45.88				

Appendix Table 6: SEM analyses (wt%) of silicate minerals in DB2 at the NFDO.

	Amphibole																								
O	52.15	53.18	53.54	53.2	55.82	52.93	53.41	52.59	52.95	53.36	52.98	52.93	53.46	53.3	53.68	54.13	54.02	54.45	53.31	53.37	54.01	54.03	53.53	53.67	54.63
Na	0.61											0.69	0.54	0.67	0.58										
Mg	5.59	6.57	6.92	6.04	5.82	5.94	5.77	5.34	5.57	5.42	3.95	6.04	5.38	5.75	6.01	5.71	6.17	5.2	4.36	7.04	6.39	6.2	6.16	5.63	5.17
Al	3.33	0.79	0.97	2.08	2.14	2.09	2.08	3.17	2.38	2.09	2.72	2.94	3.1	3.23	2.67	2.63	2.56	3.06	2.38	1.1	2.07	2.7	2.65	2.39	1.52
Si	20.05	22.36	22.09	22.01	19.57	21.87	21.66	21.24	21.6	21.26	13.4	20.24	19.52	20.08	20.94	20.8	20.63	20.35	19.01	22.3	20.9	20.56	20.95	21.29	21.05
K	0.46									0.19	0.43	0.4	0.47	0.45	0.23	0.23	0.34	0.64			0.18	0.35	0.32		
Ca	6.47	6.6	6.43	6.68	5.4	6.71	6.57	7.02	6.73	6.57	4.25	6.24	6.35	6.17	6.31	6.32	6.16	5.48	8.87	6.54	5.78	6.18	6.27	6.65	6.08
Ti	0.68										7.54	0.55	1.27	0.6	0.23	0.19	0.41		3.37	0.17		0.45	0.45		0.18
Mn						0.32					0.67										0.19				0.18
Fe	10.59	10.49	9.94	9.99	11.25	10.14	10.38	10.64	10.77	11.13	14.05	9.97	9.91	9.75	9.35	9.99	9.66	10.77	8.7	9.29	10.51	9.54	9.53	10.18	11.55
Ce																									
La																									
Nd																									

Appendix Table 7: SEM analyses (wt%) of sulfides and oxides in DB-2 at the NFDO.

	Ilmenite									Pyrite																		Apatite							
O	46.6	46.5	46.54	47.17	46.98	43.74	46.33	47.19	47.37																			49.67	49.28	50.07	50.88	49.93	50	50.58	50.72
Ca	0.41	0.32	0.4	0.37		0.26	0.3	0.27																				31.45	31.66	30.85	30.71	31.1	30.98	30.84	30.39
Ti	25.27	25.77	25.68	25.31	25.42	26.29	25.43	25.18	25.28																										
Mn	1.74	1.85	1.99	1.99	1.84	2.29	2.43	2.47	1.94																										
Fe	25.98	25.56	25.39	25.16	25.76	27.43	25.51	24.89	25.41	41.36	41.31	54.08	54.11	54.02	40.55	54.15	54.13	52.37	54.42	52.77	52.59	53.62	54.3	54.17	52.88	54.3				0.38	0.37	0.43	0.36		0.44
S										58.64	58.69	45.92	45.89	45.98	59.45	45.85	45.87	47.63	45.58	47.23	47.41	46.38	45.7	45.83	47.12	45.7									
Si																												1.01	0.85	1.17	0.68	1.01	0.8	0.92	1.13
P																												17.87	18.21	17.52	17.36	17.54	17.86	17.66	17.31

Appendix Table 8: SEM analyses (wt%) of silicate minerals in the Kentville Formation hornfelds sample from the NFDO (KF-HF).

	Chlorite						Plagioclase					Biotite			Titanite	
O	55.59	53.82	56.25	55.82	54.54	56.02	55.4	55.43	55.34	55.27	55.36	52.22	52.56	52.39	51.88	52.03
Mg	7.43	7.2	7.86	7.82	7.5	8.02						5.18	5.45	5.17		
Al	10.06	10.35	10.44	10.46	10.01	10.01	12.12	12.13	12.03	11.86	12.035	8.46	8.56	8.65	0.53	0.96
Si	11.15	14.08	11.17	11.61	12.63	11.52	23.48	23.35	23.54	23.7	23.5175	15.95	15.67	15.76	13.43	13.54
K		0.83			1.49	0.68						6.38	6.24	6.4		
Ti		0.26			0.28	0.37						1.12	1.09	1.31	18.22	17.27
Fe	15.78	13.46	14.28	14.29	13.54	13.38						10.7	10.43	10.32		
Ca							3.99	4.15	3.95	3.87	3.99				15.94	16.2
Na							5.01	4.95	5.15	5.29	5.1					

Appendix Table 9: SEM analyses (wt%) of sulfides and oxides in the Kentville Formation hornfelds of the NFDO (KF-HF).

	Ilmenite						Pyrite	
O	47.62	47.56	47.17	47.51	47.69	48.65		
Si	0.29							
Ti	24.98	25.41	25.4	25.52	25.1	24.76		
Mn	1.69	1.5	1.56	1.6	1.68	1.68		
Fe	25.14	25.54	25.86	25.37	25.54	24.9	28.76	28.8
Co	0.28							
S							40.69	40.99
Cu							30.55	30.2

Appendix Table 10: SEM analyses (wt%) of the silicate minerals of the unaltered granite sample from the SMB of the NFDO (N-11-1-G)

	Biotite					Plagioclase	K-feldspar	Chlorite	Zircon							
O	47.91	47.61	48.8	48.37	51.26	53.1	52.69	53.88	39.57	38.69	39.88	40.12	40.67	40.21	42.26	38.18
Mg	2.89	2.74	2.83	2.82	3.87			8.7								
Al	7.76	7.91	8.03	7.75	8.69	11.83	8.58	10.55								
Si	15.36	15.09	14.54	15.01	14.29	26.03	27.12	11.06	13.92	13.81	13.34	13.48	13.38	13.26	11.89	13.52
Cl	0.35	0.36	0.37	0.37												
K	7.09	6.84	6.2	6.84	5.57	0.55	10.91									
Ti	2.3	2.07	1.72	2.28												
Mn	0.33	0.33	0.35	0.37	0.3											
Fe	15.99	17.06	17.16	16.18	16.01			15.8		0.3		0.43		0.29	0.47	0.36
Na						5.5	0.7									
Ca						2.99										
Zr									46.5	46	46.79	44.78	45.95	46.24	40.15	46.65
Hf															1.11	1.29
Y															4.13	

Appendix Table 11: SEM analyses (wt%) of the oxides in the unaltered granite of the SMB from the NFDO (N-11-1-G)

	Ilmenite			Apatite		
O	42.27	46.51	40.68	41.56	42.27	41.18
Mg		2.07				
Al	0.22	5.15				
Si	0.66	8.22				
P	0.96			18.23	18.45	18.36
Cl		0.18		0.37	0.41	0.32
K		3.37				
Ca	2.34			30.47	30.71	30.79
Ti	24.75	12.19	27.79			
Mn	6.53	3.29	7.2	1.1	1.07	1.22
Fe	22.27	19.01	24.33	0.81	0.76	0.7
F				7.45	6.33	6.62

Appendix Table 12: SEM analyses (wt%) of the silicate minerals for the Cloud Lake Pluton sample from the NFDO (GR-1)

	Biotite		K-feldspar	Zircon				
O	52.85	56.11	50.99	40.21	41.32	39.32	38.65	38.86
Mg	3.94	5.92		13.29	13.11	13.45	13.61	13.46
Al	9.9	8.02	8.85					
Si	13.65	10.93	28.17					
K	1.62	1.16	11.55					
Ti	0.54	6.98						
Mn	0.2	0.22						
Fe	17.29	10.66		0.29	0.64	0.37	0.38	0.52
Na			0.44					
Zr				46.21	44.93	46.86	46.24	46.02
Hf							1.12	1.14

Appendix Table 13: SEM analyses (wt%) of the oxide minerals from the Cloud Lake Pluton sample from the NFDO (GR-1)

	Apatite					Rutile	
O	42.43	42.16	42.51	41.89	42.05	47.54	49.4
F	5.63	6.22	6.71	6.07	6.33		
P	18.23	18.4	17.98	18.43	18.34		
Cl	0.3	0.39		0.41	0.36		
Ca	30.95	30.91	32.25	31.04	31.13		0.22
Mn	1.29	1.12		1.18	1.22		
Fe	1.17	0.79		0.97	0.57	0.36	2.54
Ce			0.56				
Si						0.43	0.74
Ti						51.67	45.48
Ag							1.62

Appendix Table 14: SEM analyses (wt%) of the sulfide minerals from the granitic dyke sample in the NFDO (GDY-1).

	Pyrite					Chalcopyrite	Galena		Arsenopyrite
Si	0.26		0.33		0.16	0.21			
S	56.58	56.72	56.22	57.27	56.71	38.78	14.88	14.94	20.79
Fe	43.16	43.28	43.45	42.73	43.12	28.72			29.9
Cu						32.29			
Pb							83.96	85.06	
Co									2.04
As									47.27

Appendix Table 15: SEM analyses (wt%) of the granite breccia sample in the NFDO (GRBX).

	Rutile	
O	48.59	49.36
Al		0.37
Si	0.34	0.79
K		0.23
Ti	51.07	49
Fe		0.24

Appendix Table 16: SEM analyses (wt%) of the sulfide minerals in the brecciated quartz vein sample from MZ1 in the NFDO (MZ1-BX)

	Pyrite		
O			3.68
Si	0.24	0.22	0.26
S	56.01	56.46	53.66
Fe	42.3	42.6	41.78
As	1.46	0.71	0.63

Appendix Table 17: SEM analyses (wt%) of the sulfide and oxide minerals from the laminated quartz vein sample from MZ1 in the NFDO (MZ1-La).

	Cobaltite					Arsenopyrite		Rutile		Pyrite			
O				0.96	3.06	9.3	9.91	50.47	48.69				
Si	0.31	0.4	0.35	0.39	1.52	0.39	0.42	1.64	0.57	0.22	0.2	0.4	0.47
S	22.74	23.48	22.34	22.35	21.51	35.03	45.61			56.15	56.61	56.1	56.53
Fe	9.07	7.47	6.65	7.38	6.59	24.6	34.8		0.24	42.84	43.2	42.35	43
Co	24	26.1	25.53	24.47	23.37	12.46	1.94						
Ni					1.77	1.65							
As	43.87	42.55	45.12	44.44	42.17	16.16	6.8			0.79		0.59	
Al						0.41	0.53	0.34	0.39				
K								0.14	0.22				
Ti								47.42	49.9				
Br												0.56	

Appendix Table 18: EPMA results (wt%) from the Fe-rich arsenopyrite phase analysed in all mineralized samples at the NFDO.

	Fe	Co	Ni	As	Au	S	Bi	Sb	Total
	34.30	1.35	<0.03	42.17	<0.03	21.99	<0.03	0.11	100.07
	35.20	0.03	<0.03	43.99	<0.03	21.18	<0.03	<0.03	100.57
MZ2-1	33.22	0.53	0.17	42.35	<0.03	21.53	0.30	0.09	98.20
	33.22	0.53	0.17	42.35	<0.03	21.53	0.30	0.09	98.20
	33.75	1.42	0.03	39.53	<0.03	24.00	0.03	<0.03	98.81
	34.14	0.04	<0.03	42.02	0.03	22.10	<0.03	<0.03	98.35
MZ1-LBX	25.76	10.51	<0.03	43.86	<0.03	20.27	<0.03	<0.03	100.75
	32.84	0.91	0.46	41.32	<0.03	22.37	0.10	0.04	98.03
	33.76	0.25	0.06	43.04	<0.03	21.62	<0.03	0.03	98.76
	32.84	0.91	0.46	41.32	<0.03	22.37	0.10	0.04	98.03
	33.76	0.25	0.06	43.04	<0.03	21.62	<0.03	0.03	98.76
	33.99	0.71	<0.03	40.63	0.03	23.55	<0.03	<0.03	98.92
	33.48	0.51	<0.03	43.29	0.04	21.40	0.13	0.04	98.89
	33.71	0.90	<0.03	40.96	<0.03	23.08	0.03	0.03	98.72
	33.69	0.13	<0.03	44.11	<0.03	20.67	0.03	<0.03	98.67
	33.53	0.97	<0.03	40.65	<0.03	23.07	<0.03	0.04	98.29
MZ1-1	33.89	0.18	<0.03	43.75	<0.03	21.00	<0.03	<0.03	98.83
	27.70	4.28	2.87	41.86	<0.03	20.69	<0.03	0.06	98.55
	32.84	0.91	0.46	41.32	<0.03	22.37	0.10	0.04	98.03
	33.76	0.25	0.06	43.04	<0.03	21.62	<0.03	0.03	98.76
	33.99	0.71	<0.03	40.63	0.03	23.55	<0.03	<0.03	98.92
	33.48	0.51	<0.03	43.29	0.04	21.40	0.13	0.04	98.89
	33.71	0.90	<0.03	40.96	<0.03	23.08	0.03	0.03	98.72
	33.69	0.13	<0.03	44.11	<0.03	20.67	0.03	<0.03	98.67
	33.53	0.97	<0.03	40.65	<0.03	23.07	<0.03	0.04	98.29
	33.89	0.18	<0.03	43.75	<0.03	21.00	<0.03	<0.03	98.83
	27.70	4.28	2.87	41.86	<0.03	20.69	<0.03	0.06	98.55
	34.96	0.39	<0.03	44.49	<0.03	20.88	<0.03	<0.03	100.78
	35.12	0.59	<0.03	43.62	<0.03	21.40	<0.03	<0.03	100.85
	35.24	0.27	<0.03	44.86	<0.03	20.55	<0.03	<0.03	101.02
MZ1-Lb	34.93	0.37	<0.03	39.67	<0.03	23.48	<0.03	<0.03	99.37
	33.32	0.81	<0.03	43.20	<0.03	21.49	0.08	0.05	98.95
	34.60	0.15	<0.03	40.32	<0.03	23.50	0.04	0.03	98.65
	33.45	0.08	<0.03	44.24	0.03	20.81	0.08	0.03	98.73
	32.32	1.73	<0.03	42.59	0.03	21.75	0.09	<0.03	98.51

Appendix Table 19: EPMA analyses (wt%) of the Fe-rich cobaltite phase analysed in all mineralized samples.

	Fe	Co	Ni	O	As	Si	Te	Ag	Au	S	Bi	Sb	Total
	8.95	23.83	3.39	0.08	44.23	0.04	0.02	<0.02	<0.03	20.18	<0.06	<0.03	100.72
	10.79	25.69	0.48	0.10	43.25	0.01	<0.02	<0.02	<0.03	20.31	<0.06	<0.03	100.63
MZ2-1	9.90	25.95	0.63	0.09	43.83	0.03	<0.02	<0.02	0.04	20.52	<0.06	<0.03	100.99
	5.40	29.10	1.71	<0.03	43.48	<0.01	0.02	<0.06	<0.03	20.51	<0.12	<0.03	100.24
	6.79	28.64	1.43	<0.03	41.27	<0.01	0.01	<0.06	<0.03	21.87	<0.12	<0.03	100.03
	24.80	8.64	2.76	0.32	43.50	0.02	0.02	<0.02	<0.03	20.49	<0.05	<0.03	100.55
	29.64	7.21	0.06	0.28	42.57	<0.01	<0.02	<0.02	<0.03	21.07	<0.05	<0.03	100.85
	28.30	8.81	0.03	0.27	40.99	<0.01	<0.02	<0.02	<0.03	22.15	<0.05	<0.03	100.58
MZ1-LBX	26.22	10.17	0.07	0.32	42.66	0.02	<0.02	<0.02	<0.03	20.84	<0.05	<0.03	100.31
	16.68	18.77	<0.03	0.34	43.45	0.01	<0.02	<0.02	<0.03	20.73	0.05	<0.03	100.06
	0.72	33.40	<0.03	0.38	42.76	0.02	<0.02	<0.02	<0.03	21.65	<0.05	<0.03	99.06
	0.87	33.38	<0.03	0.37	43.37	<0.01	<0.02	<0.02	<0.03	21.44	<0.05	<0.03	99.49
	11.33	23.65	0.04	<0.03	45.29	<0.01	<0.02	<0.06	<0.03	19.96	<0.12	<0.03	100.29
MZ1-1	7.35	28.49	<0.03	<0.03	43.50	<0.01	<0.02	<0.06	<0.03	20.40	<0.12	<0.03	99.83
	8.89	26.58	0.03	<0.03	44.33	<0.01	<0.02	<0.06	<0.03	19.84	<0.12	<0.03	99.67
	8.81	26.84	<0.03	<0.03	43.41	<0.01	<0.02	<0.06	<0.03	20.00	<0.12	<0.03	99.11
	8.32	28.41	0.03	0.11	43.40	<0.01	<0.02	<0.02	<0.03	20.32	<0.06	<0.03	100.59
	9.79	25.68	0.45	0.11	44.31	0.06	<0.02	<0.02	0.03	19.85	<0.06	<0.03	100.27
	9.86	24.96	1.30	0.10	43.69	0.04	<0.02	<0.02	<0.03	20.03	<0.06	<0.03	100.00
	9.00	26.69	0.24	0.16	42.36	0.01	<0.02	<0.02	<0.03	20.34	<0.06	<0.03	98.80
	10.60	25.79	0.52	0.17	43.85	<0.01	<0.02	<0.02	<0.03	20.28	<0.06	<0.03	101.24
MZ1-Lb	5.34	31.32	0.05	0.13	42.77	<0.01	<0.02	<0.02	<0.03	20.72	<0.06	<0.03	100.35
	10.51	24.69	1.40	0.15	44.18	0.03	0.02	<0.02	<0.03	20.38	<0.06	<0.03	101.40
	10.33	26.05	0.41	0.16	43.40	0.02	<0.02	<0.02	0.03	20.78	<0.06	<0.03	101.19
	11.44	24.98	0.03	0.09	45.00	<0.01	<0.02	<0.02	<0.03	19.38	<0.06	<0.03	100.91
	10.12	26.03	<0.03	0.10	44.29	0.03	<0.02	<0.02	<0.03	19.76	<0.06	<0.03	100.34
	11.20	24.45	<0.03	<0.03	43.49	<0.01	<0.02	<0.06	<0.03	19.81	<0.12	<0.03	99.04
	9.84	25.59	<0.03	<0.03	44.37	<0.01	<0.02	<0.06	<0.03	19.75	<0.12	<0.03	99.57

Appendix Table 20: EPMA results (wt%) of the Fe- and Co-rich gersdorffite phase anlaysed in samples MZ2-1, MZ1-LBX, MZ1-Lb

	Fe	Co	Ni	O	As	Si	Te	Ag	Au	S	Bi	Sb	Total
	4.28	23.962	7.505	0.079	44.656	<0.01	0.07	<0.02	<0.03	18.837	<0.06	<0.03	99.393
	6.805	23.692	4.98	<0.03	43.829	<0.01	0.031	<0.06	<0.03	19.647	<0.12	<0.03	99.015
MZ2-1	8.096	20.97	6.809	<0.03	44.651	<0.01	0.063	<0.06	<0.03	19.683	<0.12	<0.03	100.322
	6.165	24.869	4.943	<0.03	44.744	<0.01	0.032	<0.06	<0.03	19.454	<0.12	<0.03	100.229
	7.638	20.92	7.069	<0.03	44.155	<0.01	0.068	<0.06	<0.03	19.478	<0.05	<0.03	99.33
	19.652	7.379	8.632	0.917	41.962	0.287	0.063	<0.02	<0.03	20.427	<0.05	<0.03	99.32
MZ1-LBX	21.835	4.336	9.311	0.502	46.356	0.076	0.096	<0.02	<0.03	19.438	<0.05	<0.03	101.96
	24.538	8.45	3.094	0.307	43.549	<0.01	0.028	<0.02	<0.03	20.118	<0.05	<0.03	100.087
	17.666	7.652	10.468	0.621	43.676	0.062	0.087	<0.02	<0.03	19.429	<0.06	<0.03	99.661
MZ1-Lb	4.805	27.818	3.823	0.114	44.169	0.032	0.032	<0.02	<0.03	19.586	<0.06	<0.03	100.382

Appendix Table 21: Major element concentrations (wt%) of all major lithologies sampled at the NFDO using X-ray fluorescence.

	KF	KF-HF	GB-1	DB2	GR1	GDY-1	GDY-2	Greisen	Greisen
Al_2O_3	19.04	14.97	16.54	17.86	14.84	21.22	17.78	13.83	13.80
BaO	0.05	0.04	0.03	0.06	0.05	0.02	0.05	0.04	0.04
CaO	0.61	1.90	10.24	10.13	0.26	1.56	0.98	0.65	0.65
Cr_2O_3	0.02	0.02	0.04	0.01	0.01	0.00	0.00	0.01	0.01
Fe_2O_3	7.96	7.44	12.00	12.19	2.67	3.10	2.68	2.12	2.11
K_2O	4.44	1.75	1.37	1.20	4.79	0.87	4.16	3.32	3.32
MgO	3.60	2.71	8.36	3.41	0.74	0.59	0.55	0.46	0.46
MnO	0.07	0.14	0.19	0.20	0.03	0.05	0.06	0.03	0.03
Na_2O	1.21	2.72	2.31	3.24	3.09	9.57	3.20	3.83	3.82
P_2O_5	0.07	0.10	0.26	0.53	0.14	0.35	0.13	0.12	0.12
SiO_2	59.46	65.79	45.90	47.26	72.80	62.40	69.76	75.71	75.35
TiO_2	1.04	1.25	1.94	3.12	0.33	0.08	0.32	0.24	0.24
Total	97.56	98.82	99.18	99.20	99.75	99.82	99.68	100.35	99.94

Appendix Table 22: Trace element concentrations (ppm) for all representative samples of the major lithologies at the NFDO using ICP-MS.

	D.L.	KF	KF-HF	GB-1	DB-2	DB-2 DUP	GR-1	GDY-1	GDY-2	Greisen	Greisen-DUP
Ag	0.008	0.02	0.01	0.04	0.13	0.14	<0.008	0.5	0.04	0.01	0.02
As	0.01	21.79	9.11	50.14	1.32	1.32	3.65	74.84	5.04	19.04	20.68
Au	0.0005	<0.0005	<0.0005	0.0015	<0.0005	<0.0005	0.0008	0.031	<0.0005	0.0005	0.0006
Ba	0.03	80.8	129.3	189.39	188.17	183.48	29.49	12.99	94.58	44.87	45.23
Be	0.001	1.048	0.767	0.638	0.634	0.588	2.408	2.484	1.437	0.98	0.959
Bi	0.0006	0.271	0.041	0.568	0.123	0.118	0.135	7.679	0.044	0.231	0.245
Cd	0.002	0.075	0.028	2.693	0.071	0.077	0.014	9.088	0.098	0.043	0.043
Ce	0.005	74	58.73	23.54	61.81	60.5	8.05	5.08	47.9	36.06	35.26
Co	0.004	24.009	20.621	33.575	30.864	32.622	3.705	3.411	4.081	3.304	3.244
Cr	0.03	108.78	104.78	75.93	26.29	26.87	18.66	7.64	19.25	22.4	21.81
Cs	0.001	7.5292	2.1224	13.7207	2.3474	2.3623	1.0895	0.8037	6.1081	2.2836	2.3112
Cu	0.3	25.3	6.8	45	57.8	60.4	1.1	41.2	1.4	2.9	2.8
Dy	0.0004	2.682	4.4167	1.8692	4.2419	4.2301	3.7985	1.0385	4.4861	3.2981	3.2331
Er	0.0002	1.0264	2.1676	0.8947	1.9583	1.8649	1.8512	0.6246	2.0731	1.5301	1.5353
Eu	0.0002	0.6971	0.7543	0.7883	1.2679	1.2319	0.2877	0.1032	0.3357	0.3818	0.3777
Ga	0.003	10.116	10.567	11.623	10.143	9.941	6.917	7.417	7.026	4.83	4.888
Gd	0.0006	4.2343	5.2254	2.3508	5.6838	5.4996	3.6191	0.791	4.8126	3.4858	3.4581
Hf	0.0002	0.3784	0.2494	0.2574	0.1442	0.1409	0.1892	0.4732	0.2705	0.2246	0.2342
Hg	0.006	<0.006	<0.006	<0.006	<0.006	<0.006	<0.006	0.006	<0.006	<0.006	<0.006
Ho	0.0002	0.425	0.809	0.354	0.768	0.751	0.689	0.197	0.792	0.586	0.578
In	0.0003	0.0281	0.0259	0.0585	0.031	0.0297	0.0142	0.2538	0.0278	0.0214	0.0225
Ir	0.0002	0.0004	0.0004	0.0006	<0.0002	0.0003	0.0004	<0.0002	0.0002	0.0002	<0.0002
La	0.002	34.86	26.06	10.9	28.12	27.71	3.02	1.97	21.52	15.88	15.54
Li	0.002	64.241	70.903	60.513	30.429	30.287	46.293	34.107	37.774	23.417	24.412
Lu	0.0001	0.108	0.2263	0.0954	0.18	0.1704	0.1789	0.1033	0.2089	0.1637	0.1684
Mo	0.01	1.42	0.6	1.12	1.98	1.99	0.72	0.54	1	1.78	1.72
Nb	0.0008	0.547	1.082	0.663	2.728	2.439	0.143	0.877	1.464	0.665	0.72
Nd	0.003	32.365	27.814	12.192	31.695	30.725	6.758	2.524	23.083	17.253	17.031
Ni	0.07	70.8	55.1	107.7	21.6	22.9	5.2	2.9	5.1	5.4	5
Pb	0.02	12.18	2.81	1.29	4.24	4.14	2.13	132.87	6.84	8	8.01
Pd	0.003	<0.003	<0.003	<0.003	<0.003	<0.003	<0.003	<0.003	<0.003	<0.003	<0.003
Pr	0.0007	8.544	6.989	2.942	7.697	7.472	1.268	0.666	5.962	4.397	4.312
Pt	0.0009	<0.0009	<0.0009	<0.0009	<0.0009	<0.0009	<0.0009	<0.0009	<0.0009	<0.0009	<0.0009
Rb	0.005	109.619	48.617	57.196	43.898	44.053	26.627	11.835	69.554	29.392	29.55
Rh	0.001	<0.001	<0.001	<0.001	<0.001	<0.001	0.001	0.003	0.001	<0.001	<0.001
Sb	0.003	0.185	0.2	0.383	0.305	0.297	0.168	0.373	0.099	0.1	0.107
Sc	0.007	6.944	11.458	5.831	6.071	6.07	3.243	3.088	5.845	3.03	3.008
Se	0.01	0.2	0.07	0.13	0.94	0.95	0.03	0.13	0.07	0.11	0.11
Sm	0.0007	6.089	6.012	2.575	6.47	6.218	2.899	0.841	5.278	3.985	3.818
Sn	0.03	1.08	0.99	10.11	1.59	1.54	1.02	8.2	1.72	1.46	1.49
Sr	0.02	6.09	10.05	240.42	142.68	140.45	4.5	12.44	6.24	4.22	4.2
Ta	0.0001	0.0031	0.0132	0.0212	0.0254	0.0185	0.0026	0.03	0.0063	0.0015	0.0021
Tb	0.0002	0.55	0.7676	0.334	0.7925	0.7693	0.6233	0.1597	0.7522	0.5549	0.5628
Te	0.001	0.029	0.006	0.013	0.083	0.077	0.001	0.084	0.002	0.013	0.016
Th	0.0008	10.81	9.966	1.104	3.049	2.966	11.75	4.541	10.708	9.173	9.064
Ti	0.1	1789	>2300	>2300	>2300	>2300	117.2	317.4	1596.9	508.6	499.5
Tl	0.0002	1.0173	0.261	0.5078	0.7378	0.719	0.1346	0.1775	0.3918	0.283	0.2933
Tm	0.0002	0.1302	0.2876	0.1163	0.2445	0.2299	0.2345	0.0972	0.2769	0.2043	0.2064
U	0.0004	1.4961	1.3534	0.2168	0.4086	0.402	1.4593	>30	2.7323	4.0789	3.7981
V	0.01	89.39	105.34	95.42	144.61	147.59	14.95	12.16	21.33	14.37	14.11
W	0.002	0.51	0.548	1.89	0.276	0.263	0.11	2.588	0.43	0.287	0.28
Y	0.0008	9.884	20.149	8.571	19.044	18.805	18.584	5.673	20.977	14.93	14.895
Yb	0.0002	0.7809	1.7352	0.6834	1.3603	1.2913	1.3606	0.7047	1.642	1.2723	1.2793
Zn	0.9	123.5	50	123.3	60	62.6	19.4	189.9	61	32.8	32.7
Zr	0.002	16.361	10.629	8.181	5.496	5.402	7.422	7.828	8.022	6.874	6.789

Appendix Table 23: Bulk rock data (ppm) for FAA of mineralized samples from MZ1 and MZ2 using ICP-AES.

	D.L.	MZ1-Lb	MZ2-1	MZ2-1DUP
Al	20	5292	29487	29404
Ba	1	23	179	183
Ca	25	333	469	461
Co	1	>1500	>1500	>1500
Cr	2	187	209	211
Cu	5	6	12	14
Fe	120	23440	38842	38715
K	27	690	9681	9695
Li	1	144	104	104
Mg	100	1700	7920	7933
Mn	1	45	294	293
Na	18	200	466	467
Ni	2	279	1346	1352
Pb	7	<7	7	10
Sc	0.26	0.58	4.04	4.17
Sr	4	9	10	10
Ti	1	149	1191	1176
V	1	11	121	120
Y	0.4	18	167.2	166.3
Zn	4	5	9	9

- *D.L.= detection limit

Appendix Table 24: Bulk rock data (ppm) of trace element concentrations from mineralized samples MZ1-Lb and MZ2-1 of the NFDO.

	D.L.	MZ2-Lb	MZ2-1	MZ2-1 DUP
Ag	0.2	0.29	4.73	5.41
As	0.7	>7700	>7700	>7700
Au	0.002	1.561	16.355	19.827
Bi	0.02	32.29	57.35	58.51
Cd	0.02	<0.02	0.06	0.06
Co	0.03	>1000	>1000	>1000
Cu	0.6	5	10	10
Hg	0.08	<0.08	<0.08	<0.08
In	0.002	0.035	0.051	0.043
Ir	0.003	<0.003	<0.003	<0.003
Mo	0.06	2.82	6.23	6.04
Ni	2	291	1477	1477
Pb	0.2	3.5	10.1	10.3
Pd	0.02	<0.02	<0.02	<0.02
Pt	0.005	<0.005	<0.005	<0.005
Rh	0.003	<0.003	0.006	<0.003
Sb	0.009	9.66	21.61	21.48
Se	0.2	11.2	23.9	23.1
Sn	0.06	0.2	0.5	0.5
Te	0.02	0.12	0.33	0.35
Tl	0.0006	0.139	0.411	0.412
Zn	2	4	9	8

- *D.L. = detection limit

Appendix Table 25: Wall rock analyses (e.g. biotite and chlorite) from sample MZ1-Lb

	Biotite								Chlorite					
Mg	3.17		1.4	1.52	0.97	0.52	1.84	0.95	12.32	8.66	9.64	8.64	9.46	5.46
Al	15.33	10.71	15.46	15.87	9.03	2.36	16.56	12.27	15.57	12.37	12.86	11.92	11.95	7.74
Si	23.41	24.65	24.76	26.01	34.07	43.26	25.07	31.07		17.62	17.16	18.3	14.05	17.65
S		1.17								0.26		0.35	0.67	0.84
Cl													0.26	0.51
K	5.52	4.38	7.31	7.81	4.1	1.01	8.23	6.56						
Ti														
Fe	5.04	6.65	1.54	1.26	1.38	0.99	1.63	0.68	13.85	16.77	16.91	15.77	15.54	14.25
As	1.95	7.79	1.01	0.64	1.31	1.2			5.33	1.79	0.94	2.16	7.04	12.76
O	45.59	44.65	45.13	46.9	49.14	51.57	46.66	48.47	41.74	42.54	42.48	42.87	40.69	40.22